

Development of efficient approximation methods in dynamical mean field theory for multi-degree-of-freedom systems

Ryota Mizuno,* Masayuki Ochi, and Kazuhiko Kuroki

Department of Physics, Osaka University, 1-1 Machikaneyama, Toyonaka, Osaka 560-0043, Japan

(Dated: June 4, 2022)

Although several impurity solvers in the dynamical mean field theory (DMFT) have been proposed, especially in multi-degree-of-freedom systems, there are practical difficulties arising from a trade-off between numerical costs and reliability. In this study, we re-interpret the iterative perturbation theory (IPT) from the perspective of the frequency dependence, and extend it such that costs and reliability can be compatible. From the same perspective, we also develop the methods in which the dual fermion calculation can be performed efficiently and can be combined with any impurity solver. We apply these methods to several models to evaluate their validity. We confirm that our methods show good agreements with the numerically exact continuous-time quantum Monte Carlo (CT-QMC) method in the local DMFT calculation, and can also capture important behaviors such as the pseudo gap in the DMFT + non-local calculation. In addition, the numerical costs are kept sufficiently small.

I. INTRODUCTION

Strongly correlated systems exhibit many exciting phenomena such as high-temperature superconductivity, metal-insulator transition, etc. However, it is difficult to understand these detailed mechanisms. These phenomena emerge in the region where both the perturbation expansions from the itinerant and localized pictures break down. In addition to this non-perturbative nature, we need to consider multi-orbital or multi-site degrees of freedom. Due to these complexities, these phenomena are still unresolved problems even though several decades have passed since their discovery. It is one of the central issues in the condensed matter physics to understand the strong correlation effects.

The dynamical mean field theory (DMFT) [1] is one of the most powerful methods to study the strongly correlated systems. DMFT is a method in which the lattice problem is solved non-perturbatively by mapping it onto an impurity problem. DMFT can treat the temporal fluctuation correctly and can connect the itinerant and localized limits smoothly. Although DMFT has these excellent features, it cannot describe the phenomena such as anisotropic superconductivity or pseudo gap since the spatial fluctuation is ignored. In order to resolve this problem, extensions which take into account the spatial fluctuation in DMFT have been developed [2, 3]. Further, formalisms to combine DMFT with ab-initio methods are established, and so DMFT is nowadays applied to various realistic calculations.

As mentioned above, in DMFT, the lattice problem is solved by mapping it onto an impurity problem, and how to solve the impurity model is important. Ideally, the best choice is using the numerically exact method, such as the continuous-time Quantum Monte Carlo method (CT-QMC) [4–8] or the exact diagonalization (ED) [9, 10]. However, especially in multi-degree-of-freedom systems, it is not uncommon that we cannot carry out the calculation practically due to its very high numerical costs. To avoid this practical difficulty, it is necessary to use a numerically low-cost approximation method as an im-

purity solver. The iterative perturbation theory (IPT) [11–15], which we bring up in this paper, is one of these methods.

The original IPT was developed as a very simple approximation, in which the self energy is calculated by the second-order perturbation. This self energy coincidentally reproduces the atomic (strong correlation) limit in the electron-hole symmetric case. Hence, in this condition, IPT is a highly useful method which can connect the weakly and strongly correlated regime even though it is a perturbation scheme. Later, the modified-IPT, which is an extended version for an electron-hole asymmetric case, was developed [16–18]. In this method, the self energy is parameterized so that it reproduces the exact solutions in the high-frequency and the atomic limits. By this improvement, IPT became able to be applied to the electron-hole asymmetric systems. Further improvement for multi-orbital systems has been made [19–22]. Similarly to the modified-IPT, the parameters are determined such that the self energy reproduces the high-frequency and the atomic limits. In multi-orbital systems, however, since the exact solution in the atomic limit cannot be obtained in a simple form, the self energy is determined such that it reproduces the approximate solution in the atomic limit. Hence the scope of the application of these methods are quite restricted. Also, it is hard to combine (all versions of) IPT with extensions which take into account the spatial fluctuations due to its approximation structure.

Given the above, we re-interpret IPT from the perspective of the frequency dependence of the two-particle quantities and extend the method such that it can be applied to multi-degree-of-freedom systems and also can be combined with the extensions for spatial fluctuations. Our extension is based on the finding that the above-mentioned frequency dependence of the two-particle quantities can be approximated in a simple form. By using this, we further develop a simplified version of the dual fermion method, where the numerical cost is significantly reduced. Also, we find that such an approximation form of the two-particle quantities can be estimated from the one-particle self energy. This enables us to combine the extensions for spatial fluctuation with any impurity solver.

This paper is organized as follows. In Sec. II and III, we define the models and outline the Green function method and formalisms concerning DMFT. We describe in Sec. IV the novel methods developed in the present study. Results are shown in

* mizuno@presto.phys.sci.osaka-u.ac.jp

Sec. V-Sec. VII. The discussion is presented in Sec. VIII. The conclusion is given in Sec. IX.

II. MODEL AND GREEN FUNCTION

A. definitions

We consider the Hubbard model for multi-degree-of-freedom systems described by the following Hamiltonian.

$$H = \sum_{ij} \sum_{\alpha\beta} t_{ij,\alpha\beta} c_{i\alpha}^\dagger c_{j\beta} + \frac{1}{4} \sum_i \sum_{\alpha\beta\gamma\lambda} U_{\alpha\beta\gamma\lambda} c_{i\alpha}^\dagger c_{i\lambda}^\dagger c_{i\gamma} c_{i\beta} \quad (1)$$

where the subscripts with Roman letters indicate unit cells and Greek letters the set of the degree of freedom of spin, orbital, and site. $t_{ij,\alpha\beta}$ is the hopping integral and $U_{\alpha\beta\gamma\lambda}$ is the Coulomb repulsion. $c_{i\alpha}^\dagger$ is the annihilation (creation) operator.

The n -particle Green function is defined as

$$G_{i_1, \dots, i_{2n}, \alpha_1, \dots, \alpha_{2n}}^{(n)}(\tau_1, \dots, \tau_{2n}) \\ = (-1)^n \langle T [c_{i_1 \alpha_1}(\tau_1) c_{i_2 \alpha_2}^\dagger(\tau_2) \cdots c_{i_{2n-1} \alpha_{2n-1}}(\tau_{2n-1}) c_{i_{2n} \alpha_{2n}}^\dagger(\tau_{2n})] \rangle, \quad (2)$$

where $c^{(\dagger)}(\tau) = e^{\tau H} c^{(\dagger)} e^{-\tau H}$ is the Heisenberg representation of creation (annihilation) operators. $\langle A \rangle = \text{Tr}(e^{-\beta H} A)/Z$ is the statistical average of A and $Z = \text{Tr}(e^{-\beta H})$ is the partition function.

In the presence of the time and lattice translational invariance, one-particle Green function [$n = 1$ in Eq. (2)] in the momentum space can be written as

$$G_{\alpha\beta}(\mathbf{k}, \tau) \equiv G_{\alpha\beta}^{(1)}(\mathbf{k}, \tau) = -\langle T c_{\mathbf{k}\alpha}(\tau) c_{\mathbf{k}\beta}^\dagger \rangle \quad (3)$$

where \mathbf{k} denotes the momentum. The Fourier transformation in terms of the imaginary time is expressed as

$$G_{\alpha\beta}(\mathbf{k}, \tau) = \frac{1}{\beta} \sum_n G_{\alpha\beta}(\mathbf{k}, i\omega_n) e^{-i\omega_n \tau} \quad (4)$$

$$G_{\alpha\beta}(\mathbf{k}, i\omega_n) = \int d\tau G_{\alpha\beta}(\mathbf{k}, \tau) e^{i\omega_n \tau} \quad (5)$$

where $\omega_n = (2n+1)\pi T$ with $n \in \mathbb{Z}$ is a fermionic Matsubara frequency [$\nu_m = 2m\pi T$ introduced later is a bosonic Matsubara frequency]. $G(\mathbf{k}, i\omega_n)$ can be derived in the following form.

$$G(\mathbf{k}) = [(i\omega_n + \mu)I - \epsilon_{\mathbf{k}} - \Sigma(\mathbf{k})]^{-1}, \quad (6)$$

where μ is the chemical potential and $k = (\mathbf{k}, i\omega_n)$ is the generalized fermionic momentum [$q = (\mathbf{q}, i\nu_m)$ introduced later denotes the generalized bosonic momentum]. $\epsilon_{\mathbf{k}} = N_{\mathbf{k}}^{-1} \sum_j t_{ij} e^{i(\mathbf{R}_i - \mathbf{R}_j) \cdot \mathbf{k}}$ is the band dispersion and $\Sigma(\mathbf{k})$ is the self energy.

Similarly to the one-particle case, in the presence of the time and lattice translational invariance, the two-particle Green function [$n = 2$ in Eq. (2)] in the momentum space can be written as

$$G_{\alpha\beta\gamma\lambda}^{(2)}(\mathbf{k}, \mathbf{k}', \mathbf{q}, \tau_1, \tau_2, \tau_3) = \langle T c_{\mathbf{k}\alpha}(\tau_1) c_{\mathbf{k}+\mathbf{q}\beta}^\dagger(\tau_2) c_{\mathbf{k}'\gamma}(\tau_3) c_{\mathbf{k}'\lambda}^\dagger \rangle. \quad (7)$$

Fourier transformation is given by

$$G^{(2)}(\mathbf{k}, \mathbf{k}', \mathbf{q}, \tau_1, \tau_2, \tau_3) \\ = \frac{1}{\beta^3} \sum_{m'm} G^{(2)}(\mathbf{k}, \mathbf{k}', \mathbf{q}, i\omega_n, i\omega_{n'}, i\nu_m) e^{-i\omega_n \tau_1} e^{i(\omega_n + \nu_m) \tau_2} e^{-i(\omega_{n'} + \nu_m) \tau_3}. \quad (8)$$

And the two-particle Green function can be divided into two parts : non-interacting and interacting terms.

$$G_{\alpha\beta\gamma\lambda}^{(2)}(k, k', q) \\ = G_{\alpha\beta}(k) G_{\lambda\gamma}(k') \delta_{q,0} - G_{\alpha\gamma}(k) G_{\lambda\beta}(k+q) \delta_{kk'} \\ + \sum_{\alpha'\beta'\gamma'\lambda'} G_{\alpha\gamma'}(k) G_{\lambda'\beta}(k+q) F_{\gamma'\lambda'\alpha'\beta'}(k, k', q) G_{\alpha'\gamma}(k') G_{\lambda\beta'}(k'+q) \quad (9)$$

where F is called the full vertex and includes all information of the interaction. Introducing the irreducible susceptibility

$$\chi_{0,\alpha\beta\gamma\lambda}(k, k', q) = -G_{\alpha\gamma}(k) G_{\lambda\beta}(k+q) \delta_{kk'}, \quad (10)$$

we can define the generalized susceptibility as

$$\chi_G(k, k', q) = \chi_0(k, k', q) - \chi_0(k, q) F(k, k', q) \chi_0(k', q). \quad (11)$$

Also we can write the self energy by using full vertex as

$$\Sigma(k) = \Sigma^{\text{HF}} + \frac{1}{2} \sum_{k', q} F(k, k', q) \chi_0(k', q) U G(k+q), \quad (12)$$

where Σ^{HF} is the Hartree-Fock term.

B. parquet formalism

To consider the diagrammatic structure of the full vertex F , we have to define the irreducible susceptibilities concerning the following three channels (ph, $\overline{\text{ph}}$, pp).

$$\chi_{0,\alpha\beta\gamma\lambda}(k, k', q) = \begin{cases} -G_{\alpha\gamma}(k) G_{\lambda\beta}(k+q) \delta_{kk'} & (\text{ph}) \\ G_{\alpha\beta}(k) G_{\lambda\gamma}(k') \delta_{q0} & (\overline{\text{ph}}) \\ G_{\alpha\gamma}(k) G_{\beta\lambda}(-k-q) \delta_{kk'} & (\text{pp}) \end{cases} \quad (13)$$

ph channel in Eq. (13) is the same as Eq. (10). The full vertex F can be divided into four parts,

$$F = \Lambda + \Phi_{\text{ph}} + \Phi_{\overline{\text{ph}}} + \Phi_{\text{pp}}, \quad (14)$$

where Φ_l ($l = \text{ph}, \overline{\text{ph}}, \text{pp}$) is the set of reducible diagrams in channel l , and Λ is the set of fully irreducible diagrams. The diagrammatic representation is shown in Fig. 1. Since there is no diagram which simultaneously satisfies irreducibility in two or more channels, we can write

$$F = \Gamma_l + \Phi_l \quad (15)$$

$$\Gamma_l = \Lambda + \Phi_{l_1} + \Phi_{l_2} \quad (l \neq l_1 \neq l_2) \quad (16)$$

$$\Phi_l = -\Gamma_l \chi_0 F = -\Gamma_l \chi_l \Gamma_l, \quad (17)$$

where Γ_l is the set of diagrams irreducible in channel l and is called the irreducible vertex in l . χ_l are given by

$$\chi_l = \chi_0 - \chi_0 \Gamma_l \chi_l = \chi_0 - \chi_0 F \chi_0. \quad (18)$$

From Eqs. (15)–(18), which are called the parquet equations [23–26], we can calculate F exactly if we know the exact Λ . However, it is almost impossible to obtain the exact Λ and the procedure to obtain Φ_l is numerically very expensive. Thus, some approximations or simplifications have been suggested [27–29] [see Appendix A].

III. DMFT, IMPURITY SOLVERS, AND EXTENSIONS

A. DMFT

DMFT is based on the equivalency between two models which is exact in the limit of the infinite spatial dimension $d \rightarrow \infty$. In the finite spatial dimension case, DMFT can be considered as the approximation in which the temporal fluctuation is treated correctly instead of ignoring the spatial fluctuation.

In DMFT, the lattice problem is solved by mapping it onto an impurity problem. The lattice model (Hubbard model) is given in Eq. (1). The Anderson impurity model for multi-degree-of-freedom systems is described as

$$\begin{aligned} H = & \sum_{\mathbf{k}} \sum_{\alpha\beta} \epsilon_{\mathbf{k}\alpha\beta} b_{\mathbf{k}\alpha}^\dagger b_{\mathbf{k}\beta} + \sum_{\mathbf{k}} \sum_{\alpha\beta} (V_{\mathbf{k}\alpha\beta} b_{\mathbf{k}\alpha}^\dagger f_\beta + \text{h.c.}) \\ & + \sum_{\alpha\beta} \epsilon_{f\alpha\beta} f_\alpha^\dagger f_\beta + \frac{1}{4} \sum_{\alpha\beta\gamma\lambda} U_{\alpha\beta\gamma\lambda} f_\alpha^\dagger f_\lambda^\dagger f_\gamma f_\beta, \end{aligned} \quad (19)$$

where $b_{\mathbf{k}\alpha}^{(\dagger)}$ is annihilation (creation) operator for bath electrons and $f_\alpha^{(\dagger)}$ for impurity electrons. $\epsilon_{\mathbf{k}\alpha\beta}$ and $\epsilon_{f\alpha\beta}$ are the energy of bath and impurity electrons, respectively. $V_{\mathbf{k}\alpha\beta}$ is the hybridization strength of bath and impurity electrons and $U_{\alpha\beta\gamma\lambda}$ is the interaction in the impurity site. The Green function in the Hubbard model can be written as

$$G_{\text{lat}}(\mathbf{k}) = [(i\omega_n + \mu)I - \epsilon_{\mathbf{k}} - \Sigma(i\omega_n)]^{-1}, \quad (20)$$

where the spatial fluctuation (\mathbf{k} dependence of the self energy) is ignored. Also, the Green function in the impurity model can be written as

$$G_{\text{imp}}(i\omega_n) = [(i\omega_n + \mu)I - \epsilon_f - \Delta(i\omega_n) - \Sigma(i\omega_n)]^{-1}, \quad (21)$$

where $\Delta(i\omega_n) = N_{\mathbf{k}}^{-1} \sum_{\mathbf{k}} V_{\mathbf{k}}(i\omega_n - \epsilon_{\mathbf{k}})^{-1} V_{\mathbf{k}}$ is the hybridization function. The self consistent condition in DMFT is given by

$$\Delta(i\omega_n) = (i\omega_n + \mu)I - \Sigma(i\omega_n) - \left(\sum_{\mathbf{k}} G_{\text{lat}}(\mathbf{k}) \right)^{-1}. \quad (22)$$

Although there are small differences depending on the impurity solvers, actual calculation procedure in DMFT is roughly as follows.

1. Start from an initial guess for the self energy $\Sigma(i\omega_n)$.

2. Calculate the lattice Green function $G_{\text{lat}}(\mathbf{k})$ by Eq. (21).
3. Calculate the hybridization function $\Delta(i\omega_n)$ by Eq. (22).
4. Solve the impurity problem using $\Delta(i\omega_n)$ and obtain the new self energy.
5. Go back to step 2. (iterate until convergence).

Various methods to solve the impurity problem (step 4) have been proposed [4–7, 9–16, 18–22, 30–33] and they are called impurity solvers. We introduce two impurity solvers we use in this study in the following section.

B. Impurity solvers

1. Iterative Perturbation Theory (IPT)

In the iterative perturbation theory (IPT) [11–15], the correlation part of the self energy is approximated by the second order perturbation, i.e.

$$\Sigma(i\omega_n) = \Sigma^{\text{HF}} + \Sigma^{\text{CR}}(i\omega_n), \quad (23)$$

$$\Sigma^{\text{CR}}(i\omega_n) \approx \Sigma^{2\text{nd}}(i\omega_n) = T \sum_{v_m} U \chi_0(iv_m) U G_0(i\omega_n + iv_m), \quad (24)$$

$$\chi_0(iv_m) = -T \sum_n G_0(i\omega_n) G_0(i\omega_n + iv_m), \quad (25)$$

$$G_0(i\omega_n) = [i\omega_n + \mu_0 - \Delta(i\omega_n) - \Sigma^{\text{HF}}]^{-1}, \quad (26)$$

where Σ^{HF} is the Hartree-Fock term (mean field term) and $\Sigma^{\text{CR}}(i\omega_n)$ the correlation term of the self energy, $\Delta(i\omega)$ the hybridization function, μ_0 the pseudo chemical potential. In the electron-hole symmetric case, IPT provides a good result in both weak and strong correlation regime. Especially in the strong correlation limit, the IPT self energy reproduces the exact solution even though it is a perturbation solution from the weak coupling limit. In other cases, however, the results are not so good. To overcome this weakness, modified-IPT [16, 18, 30] was proposed as an extended version of IPT for arbitrary filling. In the modified-IPT, the correlation part of the self energy is parametrized by

$$\Sigma^{\text{CR}}(i\omega_n) = \frac{A \Sigma^{2\text{nd}}(i\omega_n)}{1 - B \Sigma^{2\text{nd}}(i\omega_n)}. \quad (27)$$

The constants A and B are determined such that one reproduces the exact solutions in the high frequency and atomic limits :

$$A = \frac{n(1-n)}{n_0(1-n_0)}, \quad B = \frac{(1-2n)U + \mu_0 - \mu}{n_0(1-n_0)U^2}, \quad (28)$$

where n_0 and n are the electron numbers evaluated from $G_0(i\omega_n)$ and $G(i\omega_n)$, respectively. The chemical potential μ is determined by fixing n at the input value, while the pseudo chemical potential μ_0 is a free parameter. Various conditions for determining μ_0 have been suggested: Luttinger sum rule, $n = n_0$, etc [16, 18, 30]. Hereafter, if we write IPT, it refers to modified-IPT.

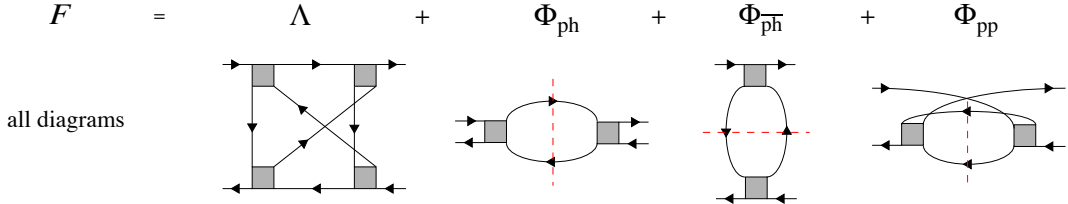


FIG. 1. The decomposition of the full vertex. The full vertex can be divided into four parts: the fully irreducible part (Λ) and the reducible parts (Φ_l , $l = \text{ph}, \text{ph}\bar{}, \text{pp}$).

Furthermore, some extended versions of the modified-IPT for multi-orbital systems have been proposed [19–22]. Here, we summarize the outline of the MO-IPT developed in Ref. [22], which is the latest version of these methods, with a slight modification. In the MO-IPT, the orbital-diagonal parts of the self energy are parametrized as

$$\Sigma_{\alpha\alpha}^{\text{CR}}(i\omega_n) = \frac{A_\alpha \Sigma_{\alpha\alpha}^{2\text{nd}}(i\omega_n)}{1 - B_\alpha \Sigma_{\alpha\alpha}^{2\text{nd}}(i\omega_n)}, \quad (29)$$

where α indicates the degrees of freedom of spin and orbital. Here, off-diagonal parts are ignored. Similarly to the single orbital case, A_α is determined such that one reproduces the exact solution in the high frequency limit. On the other hand, B_α is determined such that one reproduces the approximate solution in the atomic limit since the exact solution can not be written in a simple form in multi-orbital systems. Namely,

$$A_\alpha = \frac{1}{\tau_\alpha} \sum_{\beta \neq \alpha} U_{\alpha\beta} \langle n_\beta \rangle (1 - \langle n_\beta \rangle) U_{\beta\alpha} + \frac{1}{\tau_\alpha} \sum_{\beta \neq \alpha} \sum_{\gamma \neq \beta \neq \alpha} U_{\alpha\beta} (\langle n_\beta n_\gamma \rangle - \langle n_\beta \rangle \langle n_\gamma \rangle) U_{\gamma\alpha}, \quad (30)$$

$$B_\alpha = \frac{1}{\tau_\alpha} \left(\mu_0 - \mu - 2 \sum_{\beta (\neq \alpha)} U_{\alpha\beta} \langle n_\beta \rangle \right) + \frac{1}{\tau_\alpha^2 A_\alpha} \sum_{\beta\gamma\eta (\neq \alpha)} U_{\alpha\beta} U_{\alpha\gamma} U_{\alpha\eta} (\langle n_\beta n_\gamma n_\eta \rangle - \langle n_\beta \rangle \langle n_\gamma n_\eta \rangle), \quad (31)$$

$$\tau_\alpha = \sum_{\beta} U_{\alpha\beta} \langle n_{0\beta} \rangle (1 - \langle n_{0\beta} \rangle) U_{\beta\alpha}, \quad (32)$$

where $U_{\alpha\beta} = U_{\alpha\alpha\beta\beta}$. The difference between Eq. (31) and Eq. (A.22) in Ref. [22] is due to the difference between the notations of the zeroth-order Green function. Adopting the Matsubara frequency formalism, we impose the condition $n_{0\text{total}} = n_{\text{total}}$ to fix μ_0 , where $n_{0\text{total}}$ and n_{total} are the total electron density obtained from G_0 and G , while the real frequency is used in Ref. [22] and μ_0 is determined such that the Luttinger theorem is satisfied. We have confirmed that the results are nearly independent of the adopted frequency types or conditions for μ_0 , by performing calculations for several models studied in Ref. [22].

2. Continuous Time Quantum Monte Carlo method (CT-QMC)

The continuous time quantum Monte Carlo method (CT-QMC) [4–7, 31] is a numerically exact method using Monte

Carlo sampling. Among the several algorithms of CT-QMC, here we briefly summarize the outline of CT-HYB [5–7], which we use in this study. CT-HYB is based on the Monte Carlo summation of all imaginary time arrangements obtained from the expansion of the partition function in powers of hybridization strength V . Here, we consider the single-degree-of-freedom case for simplicity.

First, we divide the Hamiltonian of the Anderson model into the following three parts.

$$H = H_b + H_f + H_{\text{hyb}}, \quad (33)$$

$$H_b = \sum_{\mathbf{k}\sigma} \epsilon_{\mathbf{k}} b_{\mathbf{k}\sigma}^\dagger b_{\mathbf{k}\sigma}, \quad (34)$$

$$H_f = \sum_{\sigma} \epsilon_f f_{\sigma}^\dagger f_{\sigma} + U n_{\uparrow} n_{\downarrow}, \quad (35)$$

$$H_{\text{hyb}} = \sum_{\mathbf{k}\sigma} (V_{\mathbf{k}\sigma} b_{\mathbf{k}\sigma}^\dagger f_{\sigma} + \text{h.c.}), \quad (36)$$

then, we expand the partition function regarding $H_b + H_f$ as non-perturbation part, and H_{hyb} as perturbation part. Since H_b and H_f are commutable, we can calculate the statistical averages of b and f independently. Then, the terms including an odd number of b, f vanish. Therefore, the partition function can be written as

$$\frac{Z}{Z_b Z_f} = \sum_{l_1 l_1'} \int d\tau_{\uparrow} d\tau_{\uparrow}' \int d\tau_{\downarrow} d\tau_{\downarrow}' \langle P_b(q_{l_1}, q_{l_1}') \rangle_b \langle P_f(q_{l_1}, q_{l_1}') \rangle_f, \quad (37)$$

$$P_b(q_{l_1}, q_{l_1}') = V^{2(l_1+l_1')} T \prod_{\sigma} b_{\sigma}^\dagger(\tau_{l_1\sigma}) b_{\sigma}(\tau_{l_1'\sigma}) \cdots b_{\sigma}^\dagger(\tau_{1\sigma}) b_{\sigma}(\tau_{1'\sigma}), \quad (38)$$

$$P_f(q_{l_1}, q_{l_1}') = T \prod_{\sigma} f_{\sigma}^\dagger(\tau_{l_1\sigma}) f_{\sigma}(\tau_{l_1'\sigma}) \cdots f_{\sigma}^\dagger(\tau_{1\sigma}) f_{\sigma}(\tau_{1'\sigma}), \quad (39)$$

where

$$q_{l_1} = \{\tau_{1\uparrow}, \cdots, \tau_{l_1\uparrow}, \tau_{1\downarrow}, \cdots, \tau_{l_1\downarrow}\}, \quad (40)$$

$$\int_{2l_1} d\tau_{\sigma} d\tau_{\sigma}' = \frac{1}{2l_1!} \int_0^{\beta} d\tau_{l_1\sigma} \cdots d\tau_{1\sigma} d\tau_{l_1'\sigma} \cdots d\tau_{1'\sigma}, \quad (41)$$

$$Z_{b,f} = \text{Tr}(e^{-\beta H_{b,f}}), \quad (42)$$

$$\langle A \rangle_{b,f} = \frac{1}{Z_{b,f}} \text{Tr}(A e^{-\beta H_{b,f}}). \quad (43)$$

In CT-HYB, the Markov chain of the imaginary time arrangement q_{l_1} that follows the probability distribution $\langle P_b \rangle_b \langle P_f \rangle_f$ is

generated. If the quantity A_f includes only f, f^\dagger , the statistical average can be calculated as follows.

$$\begin{aligned}
\langle A_f \rangle &= \frac{1}{Z} \text{Tr}(A_f e^{-\beta H}) \\
&= \frac{\sum \int d\tau \langle P_b \rangle_b \langle P_f A_f \rangle_f}{\sum \int d\tau \langle P_b \rangle_b \langle P_f \rangle_f} \\
&= \frac{\sum \int d\tau \langle P_b \rangle_b \langle P_f \rangle_f \frac{\langle P_f A_f \rangle_f}{\langle P_f \rangle_f}}{\sum \int d\tau \langle P_b \rangle_b \langle P_f \rangle_f} \\
&\simeq \frac{1}{N_{\text{sample}}} \sum_{\{q\}}^{(\text{MC})} \frac{\langle P_f(q) A_f \rangle_f}{\langle P_f(q) \rangle_f}, \quad (44)
\end{aligned}$$

where $\sum^{(\text{MC})}$ is the sum of Monte Carlo sampling, N_{sample} is the number of samples. We can use the Wick's theorem since H_b has a quadratic form in terms of the b, b^\dagger . Then we obtain

$$\langle P_b(q_l, q'_l) \rangle_b = \prod_{\sigma} \det \Delta_{\sigma}, \quad (\Delta_{\sigma})_{ij} = \Delta_{\sigma}(\tau'_{i\sigma} - \tau_{j\sigma}), \quad (45)$$

where $\Delta_{\sigma}(\tau)$ is the hybridization function.

C. Dual fermion method

The dual fermion method [34–38] is one of the extensions of DMFT to take into account the spatial fluctuation, which is accomplished by introducing an auxiliary particle called dual fermion. In the dual fermion system, particles interact with each other by the interaction which includes the local correlation effects of the original lattice system. Although there are some differences, we can adopt the method of the diagram expansion as in the lattice systems.

1. Outline

The effective action of the Hubbard model expressed by Grassmann variables is

$$S[c, c^*] = - \sum_{nk\sigma} c_{\omega k\sigma}^* (i\omega_n + \mu - \epsilon_{\mathbf{k}}) c_{\omega k\sigma} + U \sum_i \int d\tau n_{\tau i \uparrow} n_{\tau i \downarrow}, \quad (46)$$

and the Anderson model

$$S_{\text{imp}}[c_i, c_i^*] = - \sum_{n\sigma} c_{\omega i\sigma}^* (i\omega_n + \mu - \Delta(i\omega_n)) c_{\omega i\sigma} + U \int d\tau n_{\tau i \uparrow} n_{\tau i \downarrow}. \quad (47)$$

c_i, c_i^* in Eq. (47) corresponds to f, f^* in Eq. (19) due to the equivalency in DMFT. From Eqs. (46) and (47), we can obtain

$$S[c, c^*] = \sum_i S_{\text{imp}}[c_i, c_i^*] + \sum_{nk\sigma} c_{\omega k\sigma}^* (\Delta(i\omega_n) - \epsilon_{\mathbf{k}}) c_{\omega k\sigma}. \quad (48)$$

Here, we introduce new Grassmann variables d, d^* and use the following identity

$$\begin{aligned}
&\exp(A^2 c_{\omega k\sigma}^* c_{\omega k\sigma}) \\
&= B^{-2} \int \mathcal{D}d^* \mathcal{D}d \exp[-AB(c_{\omega k\sigma}^* d_{\omega k\sigma} + d_{\omega k\sigma}^* c_{\omega k\sigma}) \\
&\quad - B^2 d_{\omega k\sigma}^* d_{\omega k\sigma}], \quad (49)
\end{aligned}$$

where A, B are complex numbers. Assuming $A^2 = \Delta(i\omega_n) - \epsilon_{\mathbf{k}}$, $B^{-2} = G_{\text{imp}}^{-2}(i\omega_n)(\Delta(i\omega_n) - \epsilon_{\mathbf{k}})^{-1}$, the partition function in the lattice system can be transformed as

$$Z = Z_d \int \mathcal{D}d^* \mathcal{D}d \mathcal{D}c^* \mathcal{D}c \exp(-S[c, c^*, d, d^*]), \quad (50)$$

$$\begin{aligned}
S[c, c^*, d, d^*] &= \sum_i S_{\text{imp}}[c_i, c_i^*] \\
&\quad + \sum_{nk\sigma} [G_{\text{imp}}^{-1}(i\omega_n)(d_{\omega k\sigma}^* c_{\omega k\sigma} + c_{\omega k\sigma}^* d_{\omega k\sigma}) \\
&\quad + G_{\text{imp}}^{-2}(i\omega_n)(\Delta(i\omega_n) - \epsilon_{\mathbf{k}})^{-1} d_{\omega k\sigma}^* d_{\omega k\sigma}], \quad (51)
\end{aligned}$$

where $Z_d = \prod_{nk} G_{\text{imp}}^2(\omega_n)(\Delta(i\omega_n) - \epsilon_{\mathbf{k}})$. The second term in the right hand side of Eq. (51) can be transformed to the real space representation since $G_{\text{imp}}(i\omega_n)$ is independent of \mathbf{k} . Therefore S is rewritten as

$$\begin{aligned}
S[c, c^*, d, d^*] &= \sum_i S_{\text{site}}[c_i, c_i^*, d_i, d_i^*] \\
&\quad + \sum_{nk\sigma} G_{\text{imp}}^{-2}(i\omega_n)(\Delta(i\omega_n) - \epsilon_{\mathbf{k}})^{-1} d_{\omega k\sigma}^* d_{\omega k\sigma}, \quad (52)
\end{aligned}$$

where

$$\begin{aligned}
S_{\text{site}}[c_i, c_i^*, d_i, d_i^*] &= S_{\text{imp}}[c_i, c_i^*] \\
&\quad + \sum_{ni\sigma} G_{\text{imp}}^{-1}(i\omega_n)(d_{\omega i\sigma}^* c_{\omega i\sigma} + c_{\omega i\sigma}^* d_{\omega i\sigma}). \quad (53)
\end{aligned}$$

The crucial point here is that the integration over the initial variables c_i, c_i^* can be performed separately for each site. Executing the integration after the Taylor expansion in terms of d, d^* , we obtain

$$\begin{aligned}
&\int \mathcal{D}c_i^* \mathcal{D}c_i \exp(-S_{\text{site}}) \\
&= Z_{\text{imp}} \exp\left(\sum_{n\sigma} G_{\text{imp}}^{-1}(i\omega_n) d_{\omega i\sigma}^* d_{\omega i\sigma}\right. \\
&\quad - \frac{1}{4} \sum_{mn'm} F_{\text{imp}}(i\omega_n, i\omega_{n'}, i\nu_m) d_{\omega i\sigma}^* d_{\omega+\nu i\sigma} d_{\omega' i\sigma'} d_{\omega'+\nu i\sigma'}^* \\
&\quad \left. + \dots\right), \quad (54)
\end{aligned}$$

where F_{imp} is the local full vertex derived by solving the impurity problem. Therefore the effective action in the dual fermion

system is given by

$$S[d, d^*] = - \sum_{nk\sigma} G_{0\text{dual}}^{-1}(k) d_{\omega k\sigma}^* d_{\omega k\sigma} + \sum_i V[d_i, d_i^*], \quad (55)$$

$$G_{0\text{dual}}(k) = (i\omega_n + \mu - \epsilon_k - \Sigma(i\omega_n))^{-1} - G_{\text{imp}}(i\omega_n), \quad (56)$$

where $V[d_i, d_i^*]$ is the last term in Eq. (54), which contains two or more sets of d_i, d_i^* . In the dual fermion system, the auxiliary particles (dual fermion) interact with each other regarding $G_{0\text{dual}}(k)$ as the non-interacting Green function and V as the interaction. This resembles the Hubbard model, but differs in the points that the interaction exhibits frequency dependence and three or more particle terms. If we can solve this dual fermion problem, we can obtain the lattice quantities through the following relations which can be derived from definitions.

$$G_{\text{lat}}^{-1}(k) = (G_{\text{imp}}(i\omega_n) + G_{\text{imp}}(i\omega_n)\Sigma_{\text{dual}}(k)G_{\text{imp}}(i\omega_n))^{-1} + \Delta(i\omega_n) - \epsilon_k, \quad (57)$$

where Σ_{dual} is the self energy in the dual fermion system.

$$F_{\text{lat}}(k, k', q) = L(k)L(k+q)F_{\text{dual}}(k, k', q)R(k')R(k'+q), \quad (58)$$

$$L(k) = G_{\text{lat}}^{-1}(k)(\Delta(i\omega_n) - \epsilon_k)^{-1}G_{\text{imp}}^{-1}(i\omega_n)G_{\text{dual}}(k), \quad (59)$$

$$R(k) = G_{\text{dual}}(k)G_{\text{imp}}^{-1}(i\omega_n)(\Delta(i\omega_n) - \epsilon_k)^{-1}G_{\text{lat}}^{-1}(k), \quad (60)$$

where G_{dual} and F_{dual} are the Green function and the full vertex in the dual fermion system, respectively.

2. Ladder approximation

Finally, we will explain the ladder approximation used in this study to solve the dual fermion problem. This corresponds to the fluctuation exchange (FLEX) approximation in the original lattice model and is an approximation which gives the leading correction to the DMFT from the perspective of $1/d$ expansion [36]. The details of the approximation is as follows.

First, we ignore the three or more particle terms in $V[d_i, d_i^*]$ of Eq. (56), namely,

$$V[d_i, d_i^*] = \frac{1}{4} \sum_{nn'm} F_{\text{imp}}(i\omega_n, i\omega_{n'}, i\nu_m) d_{i\sigma_1}^* d_{\omega'+\nu_i\sigma_2}^* d_{\omega'\sigma_3} d_{\omega+\nu_i\sigma_4}. \quad (61)$$

This enables us to apply ordinary diagram expansion method just by the replacement $U \rightarrow F_{\text{imp}}$. Further, assuming the SU(2) symmetric case, we employ the approximation in which only the ladder diagrams depicted in Fig. 2 are taken into account. Then, the self energy in the dual fermion system is obtained as follows:

$$\Sigma_{\text{dual}}(k) = \frac{1}{4} \sum_q [V_c(i\omega_n, i\omega_{n'}, i\nu_m, \mathbf{q}) + 3V_s(i\omega_n, i\omega_{n'}, i\nu_m, \mathbf{q})] G_{\text{dual}}(k+q), \quad (62)$$

$$\begin{aligned} & V_r(i\omega_n, i\omega_{n'}, i\nu_m, \mathbf{q}) \\ &= T \sum_{n''} F_{\text{imp},r}(i\omega_n, i\omega_{n''}, i\nu_m) \chi_{0\text{dual}}(i\omega_{n''}, i\nu_m, \mathbf{q}) \\ & \quad \times [2F_{\text{dual},r}(i\omega_{n''}, i\omega_{n'}, i\nu_m, \mathbf{q}) - F_{\text{imp},r}(i\omega_{n''}, i\omega_{n'}, i\nu_m)], \end{aligned} \quad (63)$$

$$\begin{aligned} & F_{\text{dual},r}(i\omega_n, i\omega_{n'}, i\nu_m, \mathbf{q}) \\ &= F_{\text{imp},r}(i\omega_n, i\omega_{n'}, i\nu_m) \\ & \quad - \sum_{n''} F_{\text{imp},r}(i\omega_n, i\omega_{n''}, i\nu_m) \\ & \quad \times \chi_{0\text{dual}}(i\omega_{n''}, i\nu_m, \mathbf{q}) F_{\text{dual},r}(i\omega_{n''}, i\omega_{n'}, i\nu_m, \mathbf{q}), \end{aligned} \quad (64)$$

where

$$\chi_{0\text{dual}}(i\omega_n, i\nu_m, \mathbf{q}) = -\frac{1}{N_k} \sum_k G_{\text{dual}}(k) G_{\text{dual}}(k+q). \quad (65)$$

Substituting this dual self energy to Eq. (57), we can obtain the Green function in the original lattice system.

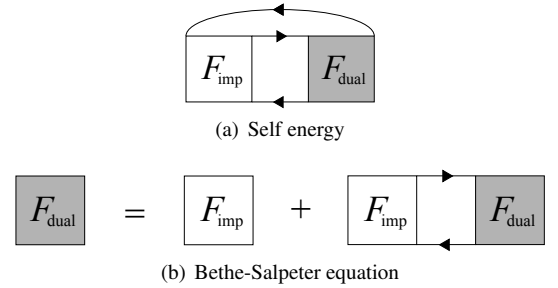


FIG. 2. The diagrammatic representation of (a) the self energy and (b) the Bethe-Salpeter equation in the dual fermion system in the ladder approximation. The bare interaction in the dual fermion system corresponds to the full vertex in the impurity system.

IV. NOVEL APPROXIMATION IN DMFT

A. The structure of full vertex

Here, we will explain the frequency structure of the full vertex [3, 24, 39]. Figure 3 shows the full vertex in the charge channel $F^c(i\omega_n, i\omega_{n'}, i\nu_m)$ in the $n-n'$ plane calculated with the QMC as the impurity solver [3, 39]. As we can see from this figure, $F^c(i\omega_n, i\omega_{n'}, i\nu_m)$ takes large values in the vicinity of the diagonal line in the $n-n'$ plane. $\overline{\text{ph}}$ and pp channels exhibit large values in the vicinity of $\omega_n - \omega_{n'} = 0$ and $\omega_n + \omega_{n'} + \nu_m = 0$, respectively. These large values on the diagonal lines come from these channels. ph channel takes large values near $\nu_m = 0$ although it is not depicted in Fig. 3. We call these structure coming from ph , $\overline{\text{ph}}$, and pp channels ‘‘diagonal structure’’.

We can also see that $F^c(i\omega_n, i\omega_{n'}, i\nu_m)$ takes large values in the vicinity of $\omega_n = 0, \omega_{n'} = 0$. These come from the combination of some channels depicted in Fig. 4 (a), which

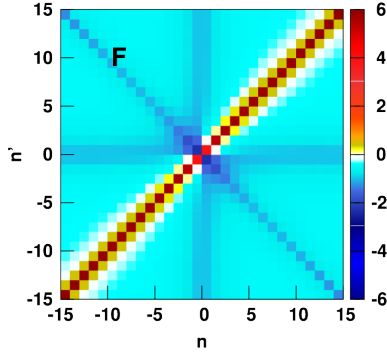


FIG. 3. The frequency dependence of the full vertex in the charge channel obtained in QMC as an impurity solver. The bare interaction U is subtracted. The calculations have been performed for the Hubbard model a square lattice with nearest-neighbor hopping t at $T/t = 0.4$, $U/t = 5.08$. The intensity is given in unit of $4t$. This figure is taken from Ref. [3].

extinguishes the ω_n or $\omega_{n'}$ dependence of $F^c(i\omega_n, i\omega_{n'}, i\nu_m)$ as follows.

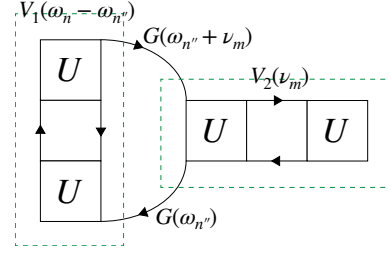
$$T \sum_{n''} V_1(\omega_n - \omega_{n''}) G(\omega_{n''} + \nu_m) G(\omega_{n''}) V_2(\nu_m) \quad (66)$$

We call these +shaped structure “cross structure”. Also, the multiple combination of some channels depicted in Fig. 4 (b) yields the contribution which depends on ω_n and $\omega_{n'}$ independently.

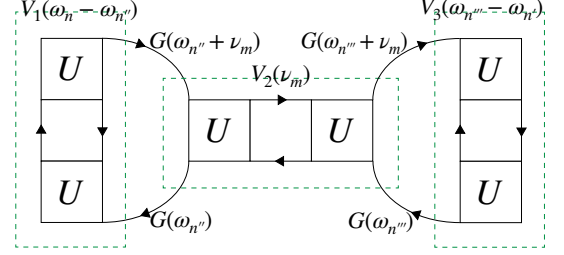
$$T^2 \sum_{n'', n'''} V_1(\omega_n - \omega_{n''}) G(\omega_{n''} + \nu_m) G(\omega_{n''}) \times V_2(\nu_m) G(\omega_{n'''} + \nu_m) G(\omega_{n'''}) V_3(\omega_{n'''} - \omega_{n'}) \quad (67)$$

Since these exhibit large values in the center of the $n - n'$ plane, we call these “central structure”. As we can see from its origin, the cross or central structures come from the higher order diagrams than that of the diagonal structure. Therefore these contributions are important in the strongly correlated regime.

In the case of single-degree-of-freedom systems, we can



(a) A diagram independent of $i\omega_{n'}$.



(b) A diagram dependent on $i\omega_n$ and $i\omega_{n'}$ independently.

FIG. 4. Examples of diagrams for each frequency structure. The diagrams depicted in (a) and (b) give the cross and central structures, respectively.

write down the full vertex in the atomic limit as follows [24].

$$F_{\text{atom}}^{c,s} = F_{\text{atom}}^{\uparrow\uparrow} \pm F_{\text{atom}}^{\uparrow\downarrow} \quad (68)$$

$$F_{\text{atom}}^{\uparrow\uparrow} = -\beta \frac{U^2}{4} (\delta_{\omega_n \omega_{n'}} - \delta_{\nu_m 0}) - \beta \frac{U^4}{16} (\delta_{\omega_n \omega_{n'}} - \delta_{\nu_m 0}) \left(\frac{1}{\omega_n^2} + \frac{1}{(\omega_{n'} + \nu_m)^2} \right) - \beta \frac{U^6}{64} \frac{\delta_{\omega_n \omega_{n'}} - \delta_{\nu_m 0}}{\omega_n^2 (\omega_{n'} + \nu_m)^2} \quad (69)$$

$$F_{\text{atom}}^{\uparrow\downarrow} = U + \beta \frac{U^2}{4} \left[\frac{2\delta_{\omega_n(-\omega_{n'} - \nu_m)} + \delta_{\nu_m 0}}{1 + e^{\beta U/2}} - \frac{2\delta_{\omega_n \omega_{n'}} + \delta_{\nu_m 0}}{1 + e^{-\beta U/2}} \right] + \frac{U^3}{8} \frac{\omega_n^2 + (\omega_n + \nu_m)^2 + (\omega_{n'} + \nu_m)^2 + \omega_{n'}^2}{\omega_n (\omega_n + \nu_m) (\omega_{n'} + \nu_m) \omega_{n'}} + \beta \frac{U^4}{16} \left[\frac{2\delta_{\omega_n(-\omega_{n'} - \nu_m)} + \delta_{\nu_m 0}}{1 + e^{\beta U/2}} \left(\frac{1}{(\omega_n + \nu_m)^2} + \frac{1}{(\omega_{n'} + \nu_m)^2} \right) - \frac{2\delta_{\omega_n \omega_{n'}} + \delta_{\nu_m 0}}{1 + e^{-\beta U/2}} \left(\frac{1}{\omega_n^2} + \frac{1}{(\omega_{n'} + \nu_m)^2} \right) \right] + \frac{3U^5}{16} \frac{1}{\omega_n (\omega_n + \nu_m) (\omega_{n'} + \nu_m) \omega_{n'}} + \beta \frac{U^6}{64} \left[\frac{2\delta_{\omega_n(-\omega_{n'} - \nu_m)} + \delta_{\nu_m 0}}{1 + e^{\beta U/2}} \frac{1}{(\omega_n + \nu_m)^2 (\omega_{n'} + \nu_m)^2} - \frac{2\delta_{\omega_n \omega_{n'}} + \delta_{\nu_m 0}}{1 + e^{-\beta U/2}} \frac{1}{\omega_n^2 (\omega_{n'} + \nu_m)^2} \right] \quad (70)$$

The structure of each order is as follows.

- $U^1 \rightarrow$ constant
- $U^2 \rightarrow$ diagonal structure
- $U^3 \rightarrow$ cross structure

- $U^4 \rightarrow$ diagonal \times cross structure
- $U^5, U^6 \rightarrow$ diagonal \times central structure

We can indeed see that the diagonal structure is dominant in the small U regime and the cross and central structures develop as U increase.

B. Extension of IPT

In this section, we reinterpret and extend the IPT from the viewpoint of the frequency dependence of the full vertex. This extension makes it easier to apply IPT to the multi-degree-of-freedom systems and to take into account the non-local correlation.

1. Full vertex in IPT

In IPT, the correlation part of the self energy is approximated as

$$\Sigma_{\text{IPT}}(\omega_n) = (1 - B\Sigma^{(2)})^{-1} A \Sigma^{(2)} \quad (71)$$

$$\Sigma^{(2)} = -T^2 \sum_{\omega_n' \nu_m} U G_0(\omega_n') G_0(\omega_n' + \nu_m) U G_0(\omega_n + \nu_m). \quad (72)$$

where A, B are the parameters which include the electron-hole asymmetry. Comparing Eq. (71) with the exact expression using the full vertex :

$$\begin{aligned} \Sigma^{\text{CR}}(\omega_n) &= -T^2 \sum_{\omega_n' \nu_m} F(\omega_n, \omega_n', \nu_m) G(\omega_n') G(\omega_n' + \nu_m) U G(\omega_n + \nu_m), \end{aligned} \quad (73)$$

the full vertex in IPT can be written as

$$F_{\text{IPT}}(\omega_n, \omega_n', \nu_m) = C_2(\omega_n) C_1(\omega_n + \nu_m) U C_1(\omega_n) C_1(\omega_n' + \nu_m) \quad (74)$$

$$C_1(\omega_n) = G_0(\omega_n) G^{-1}(\omega_n) \quad (75)$$

$$C_2(\omega_n) = (1 - B\Sigma^{(2)}(\omega_n))^{-1} A. \quad (76)$$

The diagrammatic representation of F_{IPT} is shown in Fig. 5(a). Fig. 6 (a)-(b) show the F_{atom} subtracted by terms that depend on the δ function and constant U , and (c)-(d) show F_{IPT} . We can see that these structures resemble and hence we can say that the IPT is an approximation which captures the strong correlation effects by the ‘‘pseudo’’ cross and central structures.

2. IPT+parquet method

In IPT, the full vertex has no diagonal structures while it has the pseudo cross and central structures. To take into account

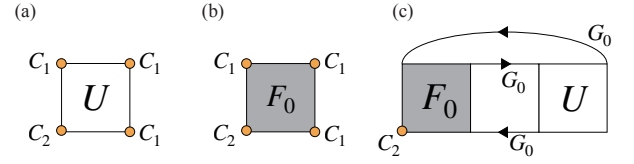


FIG. 5. Diagrammatic representation of (a) the full vertex of IPT, (b) the full vertex of IPT+parquet, and (c) the self energy,

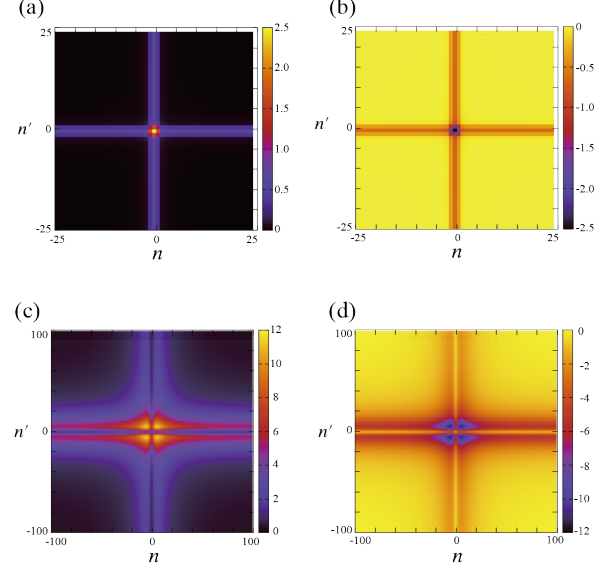


FIG. 6. The frequency dependence of the full vertex at $\nu_m = 0$. Upper panels: The frequency dependence of the full vertex in the atomic limit subtracted by the bare interaction and the terms that depend on δ function (ph, $\overline{\text{ph}}$, pp term). Lower panels: The frequency dependence of the full vertex in IPT. (a), (c) correspond to the charge channel, and (b), (d) the spin channel.

the contribution of the diagonal structures, we extend the IPT as follows.

$$\Sigma_{\text{IPT+parquet}}^{\text{CR}}(\omega_n) = C_2(\omega_n) \Sigma_0^{\text{CR}}(\omega_n) \quad (77)$$

$$\begin{aligned} (\Sigma_0^{\text{CR}}(\omega_n))_{\alpha\beta} &= -T^2 \sum_{\omega_n' \nu_m} (F_0(\omega_n, \omega_n', \nu_m))_{\alpha\beta' \lambda' \gamma'} \\ &\quad \times (G_0(\omega_n'))_{\lambda' \lambda''} (G_0(\omega_n' + \nu_m))_{\gamma' \gamma''} \\ &\quad \times U_{\lambda'' \gamma'' \beta \alpha''} (G_0(\omega_n + \nu_m))_{\beta' \alpha'} \end{aligned} \quad (78)$$

$$C_2(\omega_n) = (1 - B\Sigma_0^{\text{CR}}(\omega_n))^{-1} A \quad (79)$$

$$G_0(\omega_n) = (i\omega_n + \mu_0 - \Delta(\omega_n) - \Sigma^{\text{HF}})^{-1} \quad (80)$$

$$\begin{aligned} F_0(\omega_n, \omega_n', \nu_m) &= U + \Phi_{\text{ph}}(\nu_m) + \Phi_{\overline{\text{ph}}}(\omega_n - \omega_n') + \Phi_{\text{pp}}(\omega_n + \omega_n' + \nu_m), \end{aligned} \quad (81)$$

where F_0 is the sum of the constant and diagonal structures coming from ph, $\overline{\text{ph}}$, and pp channels. We can express this

extension in terms of the full vertex as follows.

$$\begin{aligned} & [F_{\text{IPT}}(\omega_n, \omega_{n'}, \nu_m)]_{\alpha\beta\gamma\lambda} \\ & = C_{2,\alpha\alpha'}(\omega_n)C_{1,\beta\beta'}(\omega_n + \nu_m)U_{\alpha'\beta'\gamma'\lambda'}C_{1,\gamma'\gamma}(\omega_{n'})C_{1,\lambda'\lambda}(\omega_{n'} + \nu_m) \end{aligned} \quad (82)$$

↓

$$\begin{aligned} & [F_{\text{IPT+parquet}}(\omega_n, \omega_{n'}, \nu_m)]_{\alpha\beta\gamma\lambda} \\ & = C_{2,\alpha\alpha'}(\omega_n)C_{1,\beta\beta'}(\omega_n + \nu_m) \\ & \times F_{0,\alpha'\beta'\gamma'\lambda'}(\omega_n, \omega_{n'}, \nu_m)C_{1,\gamma'\gamma}(\omega_{n'})C_{1,\lambda'\lambda}(\omega_{n'} + \nu_m) \end{aligned} \quad (83)$$

The diagrammatic representation of the self energy and full vertices are shown in Fig. 5. We need to calculate the contributions Φ_{ph} , $\Phi_{\overline{\text{ph}}}$, and Φ_{pp} in some way. Not to lose the advantage of IPT, a method with low numerical cost is desirable. To meet these requirements, we employ the simplified parquet method in Ref. [27] explained in Appendix A. Hence, we call this ‘‘IPT+parquet method’’. In this method, we can obtain $F_0 = (F_c + 3F_s)/4$, where F_c, F_s is defined in Eqs. (A6),(A7). Since the simplified parquet method in Ref. [27] has not been extended for multi-degree-of-freedom systems, we extend it for our purpose. Although the outline is almost the same as the single-degree-of-freedom case explained in Appendix A, there are some differences. The constant multiplication in Eq. (A18) implies to multiply all elements of the interaction matrix by z_r , and the summation in Eq. (A20) is replaced by the trace as follows.

$$z_r = 1 + \frac{\text{Tr}[\chi_0(k, q)(\gamma_r^{(1)}(k - k') + \gamma_r^{(2)}(k + k' + q))\chi_0(k', q)]}{\text{Tr}[\chi_0(q)\Lambda_r\chi_0(q)]} \quad (r = \text{c, s, e, o}), \quad (84)$$

where $\text{Tr}A = \sum_{k,k',q} \sum_{\alpha} A_{\alpha\alpha\alpha\alpha}(k, k', q)$ and c, s, e, and o indicate charge, spin, even, and odd channels.

The remaining problem here is how to deal with the parameters A, B , and μ_0 in the multi-degree-of-freedom systems. In MO-IPT [21, 22], the two- or more particle effects are added in the form of the static correlation functions when the single-orbital IPT is extended to the multi-orbital one as shown in Sec. III B 1. By contrast, in our formalism, these effects are already considered in the form of the diagonal terms of the dynamical full vertex obtained by the parquet equations. Therefore, we simply extend the single-orbital representation of parameters Eq. (28) to multi-orbital forms, as follows.

$$A_{\alpha\beta} = \delta_{\alpha\beta} \quad (85)$$

$$B_{\alpha\beta} = \delta_{\alpha\beta} \frac{N_{\text{orbital}}^{-1} \sum_{\gamma} U_{\alpha\alpha\gamma\gamma}(1 - 2n_{\gamma}) + \mu_{0\alpha} - \mu}{\sum_{\gamma} U_{\alpha\alpha\gamma\gamma}n_{0\gamma}(1 - n_{0\gamma})U_{\gamma\gamma\alpha\alpha}}, \quad (86)$$

where $n_{\alpha}, n_{0\alpha}$ is the band filling evaluated from G, G_0 . Here, we add a degree of freedom to the pseudo chemical potential μ_0 in order to satisfy the condition $n_{\alpha} = n_{0\alpha}$, and so A is fixed to unity. This condition is needed for the following reason. From the viewpoint of the frequency dependence of the full vertex, the correction factor $C_1 = G_0G^{-1}$ captures the strong correlation effects. Hence, C_1 needs to increase in the appropriate regions of filling, namely, in the vicinity of half

filling. In the multi-degree-of-freedom case, if μ_0 has only one element, $n_{0\alpha}$ is different from n_{α} in general even if $\sum_{\alpha} n_{0\alpha} = \sum_{\alpha} n_{\alpha}$ is satisfied. When $n_{0\alpha}$ is away from half filling, C_1 does not increase even if n_{α} is at half filling. Therefore, we need to add a degree of freedom to μ_0 for the condition $n_{\alpha} = n_{0\alpha}$.

3. Validity and Advantage

Finally, we discuss the validity and the advantage of the IPT+parquet method. The full vertex in the IPT+parquet method is represented by a simple product of functions as in Eqs. (81) and (83). Considering the fact that the two-particle fluctuations are large in the low energy region, we can find that this approximation in terms of the frequency dependence is not so bad. For example, $V_i(\nu_m)$ in Eq. (66) or Eq. (67) has a large value in the vicinity of $\nu_m = 0$. As an extreme case, if we approximate V_1 and V_3 by the δ function in Eq. (66) or Eq. (67), we obtain the frequency dependence of ph part in Eq. (83). We can also see this type of frequency dependence in the representation of the full vertex in the atomic limit in Eqs. (69),(70).

Comparing with the existing IPT formalisms, the IPT+parquet method has the following advantages. (i) In the IPT+parquet method, the dynamical effects of the two-particle fluctuation, which are more important in the multi-degree-of-freedom systems, are taken into account, whereas only the static effects are treated in the IPT. (ii) It is easy to apply diagrammatic extensions of DMFT for the non-local correlation. In the IPT+parquet method, since the two-particle fluctuations in each channel (ph, $\overline{\text{ph}}$,pp or charge,spin,even,odd) in the full vertex are estimated with a physically reasonable method (the parquet formalism), we can calculate the two-particle quantities necessary for diagrammatic extensions from this full vertex. On the contrary, in the IPT, since there is no perspective about the two-particle fluctuations in the full vertex, it is difficult to estimate the two-particle quantities. Although the method to reconstruct the full vertex in IPT has been suggested in the single-degree-of-freedom systems [40], it can not be used in the multi-degree-of-freedom systems.

C. Efficient Dual Fermion (EDF)

In the previous section, we have developed a numerically efficient impurity solver for multi-degree-of-freedom systems. To take into account the spatial fluctuation while keeping efficiency, here, we propose a numerically efficient (low-cost) approximation in the dual fermion method. Since the full vertex in the IPT+parquet is obtained in the form of Eq. (83), we focus on cases where the full vertex can be obtained in the

following form.

$$F(\omega_n, \omega_{n'}, \nu_m) \approx C_1(\omega_n)C_2(\omega_n + \nu_m)F_0(\omega_n, \omega_{n'}, \nu_m)C_3(\omega_{n'})C_4(\omega_{n'} + \nu_m) \quad (87)$$

$$F_0(\omega_n, \omega_{n'}, \nu_m) = \Lambda + \Phi_{\text{ph}}(\nu_m) + \Phi_{\text{ph}}^-(\omega_n - \omega_{n'}) + \Phi_{\text{pp}}(\omega_n + \omega_{n'} + \nu_m), \quad (88)$$

First, we omit the $\overline{\text{ph}}$ and pp parts in Eq. (88) for low-cost calculation. Hence, F_{imp} in Sec. III C is approximated as

$$F_{\text{imp}}(\omega_n, \omega_{n'}, \nu_m) \approx C_1(\omega_n)C_2(\omega_n + \nu_m)\gamma(\nu_m)C_3(\omega_{n'})C_4(\omega_{n'} + \nu_m) \quad (89)$$

$$\gamma(\nu_m) = \Lambda + \Phi_{\text{ph}}(\nu_m). \quad (90)$$

We apply the ladder approximation in the dual fermion system. By moving the correction factor $C(\omega_n)$ from the full vertex F_{imp} to the dual Green function G_{dual} , we define the following Green function-like and susceptibility-like quantities.

$$\tilde{G}^{C_i}(k) = C_i(\omega_n)G_{\text{dual}}(k) \quad (91)$$

$$\tilde{G}^{C_{ij}}(k) = C_i(\omega_n)G_{\text{dual}}(k)C_j(\omega_n) \quad (92)$$

$$\tilde{\chi}_0^C(q) = - \sum_q \tilde{G}^{C_{13}}(k)\tilde{G}^{C_{42}}(k+q) \quad (93)$$

Similarly, the charge and spin susceptibility-like quantities can be obtained as

$$\tilde{\chi}_r^C(q) = \tilde{\chi}_0^C(q)[1 + \gamma_r(\nu_m)\tilde{\chi}_0^C(q)]^{-1} \quad (r = c, s). \quad (94)$$

With these, we can obtain the dual self energy as follows.

$$\tilde{\Sigma}(k) = \frac{1}{4} \sum_q C_1(\omega_n)[V_c(q) + 3V_s(q)]\tilde{G}^{C_{24}}(k+q)C_3(\omega_n) \quad (95)$$

$$V_r(q) = 2\gamma_r(\nu_m)\tilde{\chi}_r^C(q)\gamma_r(\nu_m) - \gamma_r(\nu_m)\tilde{\chi}_0^C(q)\gamma_r(\nu_m) \quad (96)$$

As one can see, owing to the approximation of Eq. (89), we do not have to treat all three frequencies practically. The numerical cost is reduced as $O(N_\omega^3) \rightarrow O(N_\omega)$, where N_ω is the number of the mesh of the frequency. We will call this method ‘‘efficient dual fermion (EDF)’’. In the actual calculation, we find that the correction factors which remain without being integrated out such as C_1 and C_3 in Eq. (95) give an unphysical result when they are obtained in the form of Eq. (75). Therefore, when we combine EDF with IPT+parquet, we omit C_3 in Eq. (95) to avoid this problem. [When we combine EDF with IPT+parquet, C_1 in Eq. (95) corresponds to C_2 in Eq. (76). This does not give an unphysical result since this is the modified factor in IPT.]

D. Self energy to Full vertex (S2F)

As mentioned, EDF can be used when the full vertex is obtained in the form of Eq. (87) and Eq. (88). Here, we

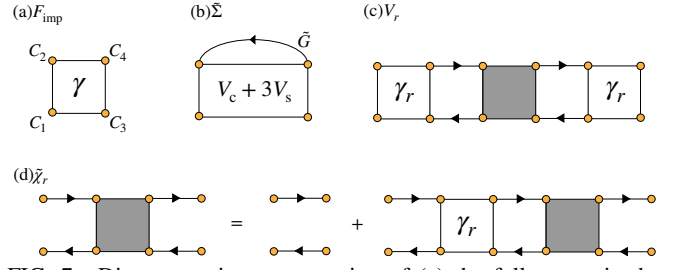


FIG. 7. Diagrammatic representation of (a) the full vertex in the impurity system, (b) the correlation part of the self energy in the dual system, (c) the function V_r , and (d) $\tilde{\chi}_r$ in the EDF method.

show that such an approximate form of the full vertex can be determined from the self energy provided that the latter is obtained. This enables us to apply diagrammatic extensions of DMFT to impurity solvers in which it is difficult to estimate the two-particle quantities.

First, we assume that the self energy is already obtained. We approximate the full vertex in the form given in Eqs. (87) and (88) and assume $C_1 = C_2 = C_3 = C_4 \equiv C$. The correlation part of self energy can be written as

$$\Sigma^{\text{CR}}(\omega_n) = -T^2 \sum_{n',m} F(\omega_n, \omega_{n'}, \nu_m)G(\omega_{n'})G(\omega_{n'} + \nu_m)UG(\omega_n + \nu_m). \quad (97)$$

From Eqs. (87),(97), we can obtain

$$\Sigma^{\text{CR}}(\omega_n) = C(\omega_n)X(\omega_n) \quad (98)$$

$$X(\omega_n) = -T^2 \sum_{n',m} C(\omega_n + \nu_m)F_0(\omega_n, \omega_{n'}, \nu_m)C(\omega_{n'}) \times G(\omega_{n'})C(\omega_{n'} + \nu_m)G(\omega_{n'} + \nu_m)UG(\omega_n + \nu_m). \quad (99)$$

Therefore, we can estimate C in the following steps: (i) calculate F_0 . (ii) calculate X by Eq. (99). (iii) obtain C by $C = \Sigma^{\text{CR}}X^{-1}$. (iv) Go back to (ii) (iterate until convergence). We will call this method ‘‘S2F (Self energy to Full vertex)’’. When we perform EDF calculation using the full vertex obtained by S2F, we omit C_1 and C_3 in Eq. (95) to avoid an unphysical result for the same reason as mentioned in Sec. IV C.

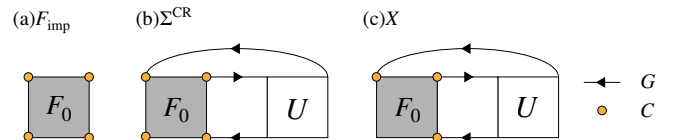


FIG. 8. Diagrammatic representation of (a) the full vertex, (b) the correlation part of the self energy, and (c) the function X in the S2F method.

V. RESULTS OF IPT+PARQUET

In this section, we show the results of IPT+parquet method. We use the quasi-particle weight as a probe of the correlation

effects. The quasi-particle weight is defined as

$$Z_\alpha = \left(1 - \frac{\text{Im}\Sigma_{\alpha\alpha}(\omega_n)}{\omega_n} \Big|_{\omega_n \rightarrow 0} \right)^{-1}. \quad (100)$$

Z_α is roughly proportional to the inverse of the effective mass, and $Z_\alpha = 0$ corresponds to the insulating state. In this study, however, we adopt the following definition instead of Eq. (100) for calculational simplicity.

$$Z_\alpha = \left(1 - \frac{\text{Im}\Sigma_{\alpha\alpha}(\omega_n)}{\omega_n} \Big|_{n=0} \right)^{-1}. \quad (101)$$

Also, in this study, we adopt the definition of the band-filling $n_\alpha (= T \sum_n G_{\alpha\alpha}(i\omega_n) e^{-i\omega_n 0})$ as the number of electrons per site per spin.

A. Single-degree-of-freedom model

We study the square lattice model as a benchmark in the single-degree-of-freedom systems. We set the temperature $T/t = 0.04$ and we take 64×64 k -meshes and 4096 Matsubara frequencies, where t is the nearest neighbor hopping. Figure 9 shows the quasi-particle weight calculated by several methods as a function of (a) the interaction U and (b) the band-filling n . IPT+FLEX is the method in which F_0 in Sec. IV B 2 is obtained by the FLEX approximation, namely, we fix z_r ($r = c, s, e, o$) to 1 in Eq. (84). In CT-QMC calculation, we use the CTHYB [7, 41–45] code based on the TRIQS library[46]. As we can see, the result of IPT+parquet is the closest to that of the numerically exact CT-QMC, since the two-particle fluctuations are underestimated in IPT and overestimated in IPT+FLEX. This quantitative improvement from (conventional) IPT is purely due to adding the diagonal terms estimated by parquet equations since the modified parameters are the same ($A = 1, B = 0$) in both IPT and IPT+parquet. In Fig. 9 (b), Z 's calculated by IPT, IPT+parquet, and CT-QMC are plotted as functions of the band filling n for $U/t = 4, 8, 12$. In the region away from half-filling, IPT+parquet tends to underestimate Z (overestimate the correlation effect) compared to IPT.

B. Two-orbital model

Here, we study the two-orbital (single-site) model. The one body part of the Hamiltonian is expressed as

$$H_0 = \sum_{ij} \sum_{\alpha\beta} t_{ij,\alpha\beta} c_{i\alpha}^\dagger c_{j\beta} - \mu \sum_i \sum_\alpha n_{i\alpha}. \quad (102)$$

The interaction part of the Hamiltonian is expressed as

$$H_{\text{int}} = \sum_l U n_{l\uparrow} n_{l\downarrow} + \sum_{l_1 \neq l_2} \sum_{\sigma_1 \sigma_2} U' n_{l_1 \sigma_1} n_{l_2 \sigma_2} + \sum_{l_1 l_2} J \mathbf{S}_{l_1} \cdot \mathbf{S}_{l_2} + \sum_{l_1 l_2} J' c_{l_1 \uparrow}^\dagger c_{l_2 \downarrow}^\dagger c_{l_2 \downarrow} c_{l_1 \uparrow}, \quad (103)$$

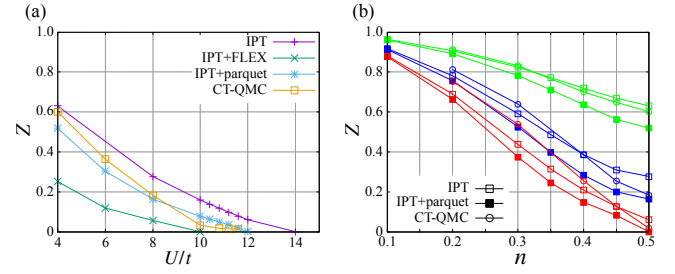


FIG. 9. Comparison of quasi-particle weight among methods. (a) The violet, blue, green and yellow lines indicate Z at half filling obtained by IPT, IPT+FLEX, IPT+parquet and CT-QMC, respectively. (b) The green, blue and red lines indicate Z for $U/t = 4, 8, 12$, respectively. The open square corresponds to modified-IPT, solid square IPT+parquet, and the circle CT-QMC. The temperature is $T/t = 0.04$ in both figures.

where the degrees of freedom of orbital are expressed by l and spin by σ . $U^{(\prime)}$ is the intra (inter)-orbital interaction, and J and J' represent the Hund's coupling and pair hopping, respectively. Then, the interaction matrices in the charge and spin channels are expressed as

$$\left(U_{l_1 l_2 l_3 l_4}^c, U_{l_1 l_2 l_3 l_4}^s \right) = \begin{cases} (U, U) & (l_1 = l_2 = l_3 = l_4) \\ (2U' - J, J) & (l_1 = l_2 \neq l_3 = l_4) \\ (2J - U', U') & (l_1 = l_3 \neq l_2 = l_4) \\ (J', J') & (l_1 = l_4 \neq l_2 = l_3) \end{cases}. \quad (104)$$

Figure 10 shows the non-interacting density of states of the models which we study here.

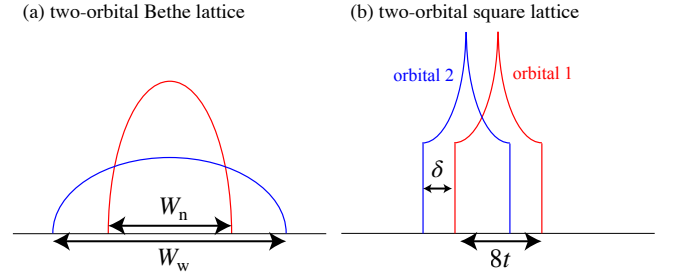


FIG. 10. The non-interacting density of states of the models: Left and right panels show the density of states of two-orbital Bethe lattice, two-orbital square lattice, respectively.

1. Two-orbital Bethe lattice

We consider the two-orbital Bethe lattice model in which two bands with different band width exist. We set $W_w/W_n = 2$, where W_n and W_w represent the half band width of the narrow and wide bands, respectively. We also set $U' = U - 2J, J = U/4, J' = 0$, and the temperature $T/W_n = 0.02$. We take 2000 real-frequency meshes and 4096 Matsubara frequencies. The quasi-particle weight against the interaction U for each orbital is plotted in Fig. 11. (a) is the result of IPT+parquet and (b) is that of the projective-QMC (PQMC) in Ref. [47]. We can

see a good agreement between the two methods. The orbital selective Mott transition, in which the energy gap opens in the narrow band whereas the wide band is still metallic, occurs at $U/W_n \sim 2.7$.

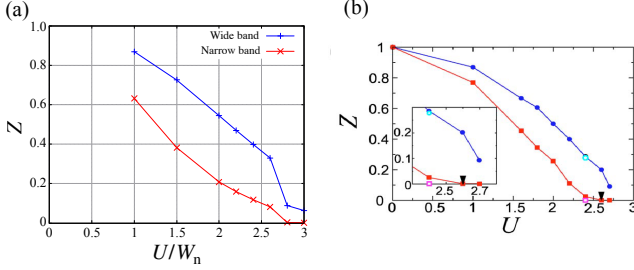


FIG. 11. Quasi-particle weight Z of the two-orbital Bethe lattice as a function of the interaction U . The temperature is $T/W_n = 0.02$. The result of IPT+parquet is shown in (a), and projective-QMC in (b)[This figure is taken from Ref. [47]]. Red and blue lines indicate the narrow band and wide band, respectively.

2. Two-orbital square lattice

We study the two-orbital square lattice model which has only the intra-orbital nearest neighbor hopping. Here, we compare three impurity solvers: IPT+parquet, CT-QMC, and MO-IPT. In the CT-QMC calculation, we use the CTHYB package [7, 41–45] based on the TRIQS library [46]. In MO-IPT calculation, the spin-flip and the pair-hopping processes are ignored since MO-IPT supports only the density-density type interactions [22]. We set $t_1 = t_2 = t$, where $t_\alpha = t_{i,i+1,\alpha}$ is the nearest neighbor hopping of orbital α and t is the unit of energy. The onsite energy difference $\delta = t_{ii,11} - t_{ii,22}$, and the interactions $U' = U - 2J$, $J = J' = U/4$. We take 32×32 k -meshes and 4096 Matsubara frequencies and we fix the temperature $T/t = 0.2$. Here, we have intentionally omitted the calculation result for half-filling, which turns out to require special care due to spontaneous symmetry breaking. This point

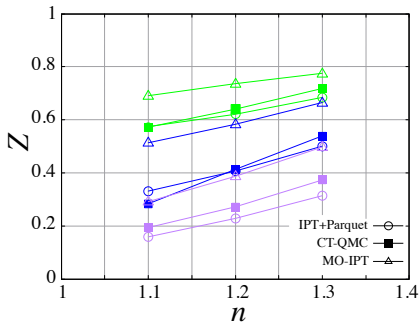


FIG. 12. Quasi-particle weight Z of the two-orbital square lattice as a function of the band filling n . The temperature is $T/t = 0.2$ and the onsite energy difference is $\delta/t = 0$. Green, blue, and purple lines indicate the results at $U/t = 4, 6, 10$, respectively. Circle, square, and triangle represent IPT+parquet, CT-QMC, and MO-IPT, respectively.

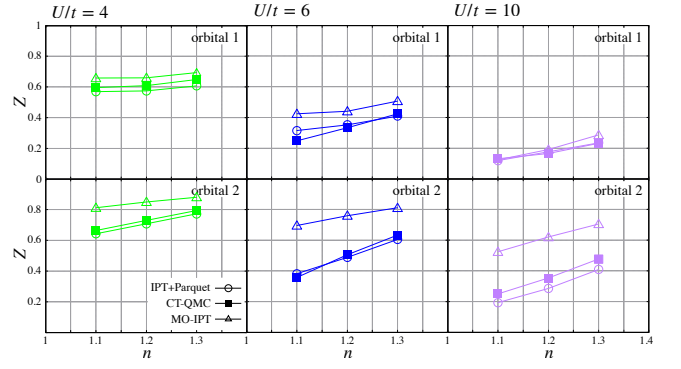


FIG. 13. Quasi-particle weight Z of the two-orbital square lattice as a function of the band filling n . The temperature is $T/t = 0.2$ and the onsite energy difference is $\delta/t = 1.6$. Green, blue, and purple lines indicate the results at $U/t = 4, 6, 10$, respectively. Circle, square, and triangle represent IPT+parquet, CT-QMC, and MO-IPT, respectively.

will be studied in detail in a separate publication.

We start with the $\delta = 0$ case (orbital degenerate case). Figure 12 shows the quasi-particle weight Z obtained by three methods MO-IPT, IPT+parquet, and CT-QMC as a function of the filling n for several interaction strength U at $\delta = 0$. Since the two orbitals are equivalent at $\delta = 0$, we show only Z of orbital 1 and omit the orbital index. The MO-IPT results significantly deviate from those of CT-QMC, which is qualitatively consistent with the situation for the two-orbital Bethe lattice model in Ref. [22]. By contrast, Z of IPT+parquet agrees well with that of CT-QMC.

We move on to the $\delta/t = 1.6$ case (orbital non-degenerate case). Figure 13 shows the quasi-particle weight Z at $\delta/t = 1.6$. The deviations of Z 's of MO-IPT from that of CT-QMC are largely different between the two orbitals [48]. IPT+parquet is found to improve the situation. This improvement comes from adding the degree-of-freedom to the pseudo chemical potential μ_0 , which enables the IPT+parquet method to capture the strong correlation effects more appropriately in both orbitals as explained in Sec. IV B. Figure 14 (a) shows the correlation part of the self energy $\Sigma^{\text{CR}}(i\omega_n)$ obtained by these three methods. We can see that $\Sigma^{\text{CR}}(i\omega_n)$ of IPT+parquet shows better agreement with CT-QMC than MO-IPT, not only in orbital 2 but also in orbital 1, and not only in the imaginary part which contributes the quasi-particle weight Z but also in the real part. Figure 14 (b)-(c) show the spectral function $A(\omega)$ obtained by performing the analytic continuation with Padé approximation in IPT+Parquet and MO-IPT, and with Maximum entropy method using the Ω Maxent code [49] in CT-QMC. Similarly to $\Sigma^{\text{CR}}(i\omega_n)$, $A(\omega)$ of IPT+parquet shows better agreement with that of CT-QMC. Especially at $n = 1.1$, IPT+parquet shows an improvement from MO-IPT.

C. Two-site model

Here, we study the bilayer model on the square lattice as a benchmark of systems with multiple sites (with one orbital per site) in a unit cell. The Hamiltonian of this model is expressed

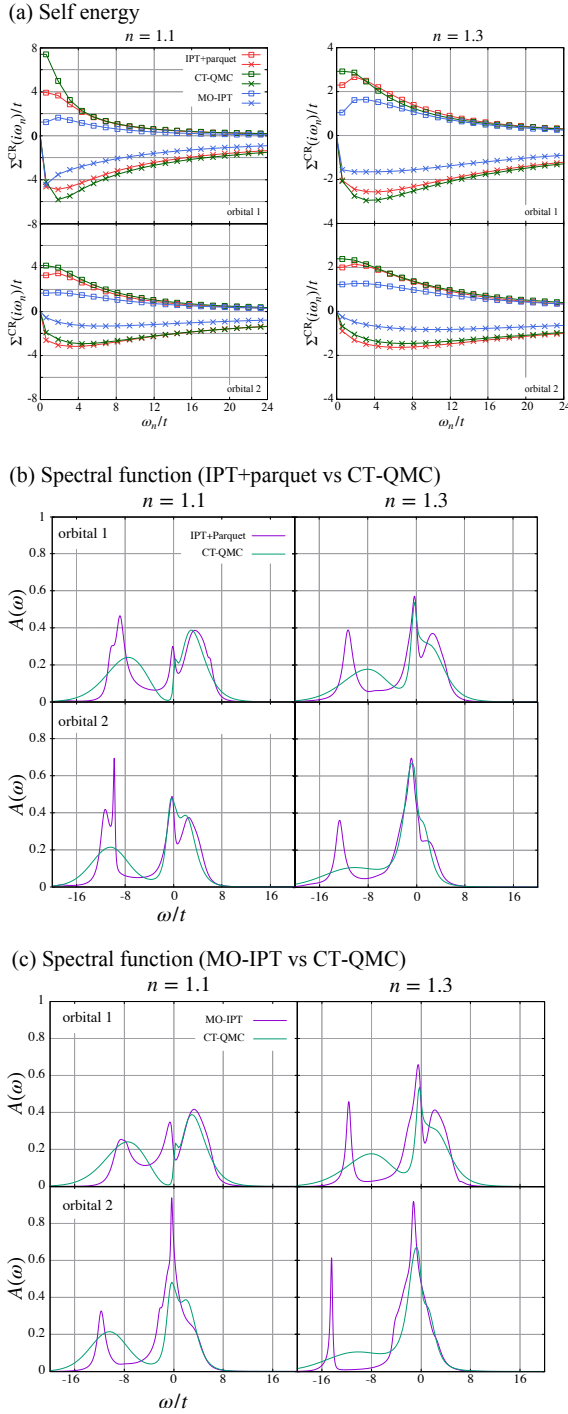


FIG. 14. (a) The correlation part of the self energy $\Sigma^{\text{CR}}(\omega)$ of the two-orbital square lattice. $\Sigma^{\text{CR}}(i\omega_n)$ of orbital 1 is shown in upper panel and orbital 2 in lower panel. Square and cross symbols indicate the real and imaginary parts, respectively. Red, green, and blue lines indicate $\Sigma^{\text{CR}}(i\omega_n)$ obtained by IPT+parquet, CT-QMC and MO-IPT, respectively. (b)(c) Spectral function $A(\omega)$ of the two-orbital square lattice for several fillings. Interaction strength is $U/t = 10$. The spectral function $A(\omega)$ of orbital 1 is shown in upper panel and orbital 2 in lower panel. Purple lines indicate $A(\omega)$ obtained by (b) IPT+parquet and (c) MO-IPT. Green lines indicate $A(\omega)$ obtained by CT-QMC. The temperature is $T/t = 0.2$, and the onsite energy difference is $\delta/t = 1.6$.

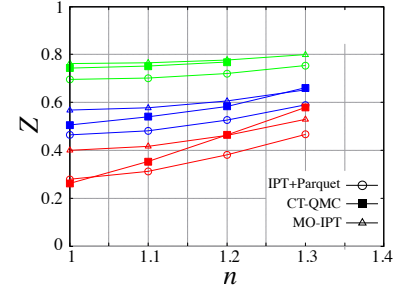


FIG. 15. Quasi-particle weight Z of the bilayer model as a function of the interaction n . Green, blue, and red lines indicate the results at $U/t = 4, 6, 8$, respectively. Circle, square, and triangle represent IPT+parquet, CT-QMC, and MO-IPT, respectively.

as

$$H = \sum_{\langle ij \rangle} \sum_{\alpha} t c_{i\alpha}^{\dagger} c_{j\alpha} + \sum_i \sum_{\alpha \neq \beta} t_{\perp} c_{i\alpha}^{\dagger} c_{i\beta} + \sum_i \sum_{\alpha} U n_{i\alpha} n_{i\alpha}, \quad (105)$$

where t (t_{\perp}) represents the intra (inter)-layer hopping and U the on-site interaction, The temperature is fixed as $T/t = 0.2$, and the hopping ratio $t_{\perp}/t = 1.0$. We take 32×32 k -meshes and 4096 Matsubara frequencies. Since the two sites are equivalent in this model, we show only the quantities of site 1 and omit the site index. The quasi-particle weight Z is plotted in Fig. 15. When $U/t = 4$, MO-IPT shows better agreement with CT-QMC than IPT+parquet. When U is increased, we can see the tendency that CT-QMC agrees with IPT+parquet (MO-IPT) near (away from) half-filling, similarly to the single-degree-of-freedom case in Sec. V A. Figure 16(a) shows the correlation part of the self energy $\Sigma^{\text{CR}}(i\omega_n)$ with $U/t = 8$. As we can also see from Z , IPT+parquet shows better agreement with CT-QMC at $n = 1.0$. At $n = 1.2$, the agreement between MO-IPT and CT-QMC is better in imaginary part whereas the agreement between IPT+parquet and CT-QMC is better in real part. In this model, the modified parameters μ_0, A, B are the same between IPT+parquet and MO-IPT since the two sites are equivalent and only the onsite interaction is considered [the interaction matrix has no off-diagonal part in terms of degree-of-freedom]. So the differences come from the two-particle fluctuation and the off-diagonal part of self energy, which are not considered in MO-IPT. Figure 16 (b)-(c) show the spectral function $A(\omega)$ with $U/t = 8$. IPT+parquet shows better agreement with CT-QMC at $n = 1.0$. At $n = 1.2$, CT-QMC and MO-IPT show better agreement in terms of the width of the central peak whereas CT-QMC and IPT+parquet show better agreement in terms of the shape of $A(\omega)$. This reflects the fact that the imaginary part of the Matsubara self energy is mainly related to the strength of renormalization [width of the central peak of $A(\omega)$] and the real part is related to the electron-hole asymmetry.

D. Scopes of applications of MO-IPT and IPT+parquet

Here, we discuss the scopes of application of MO-IPT and IPT+parquet from the results of this study and the previous

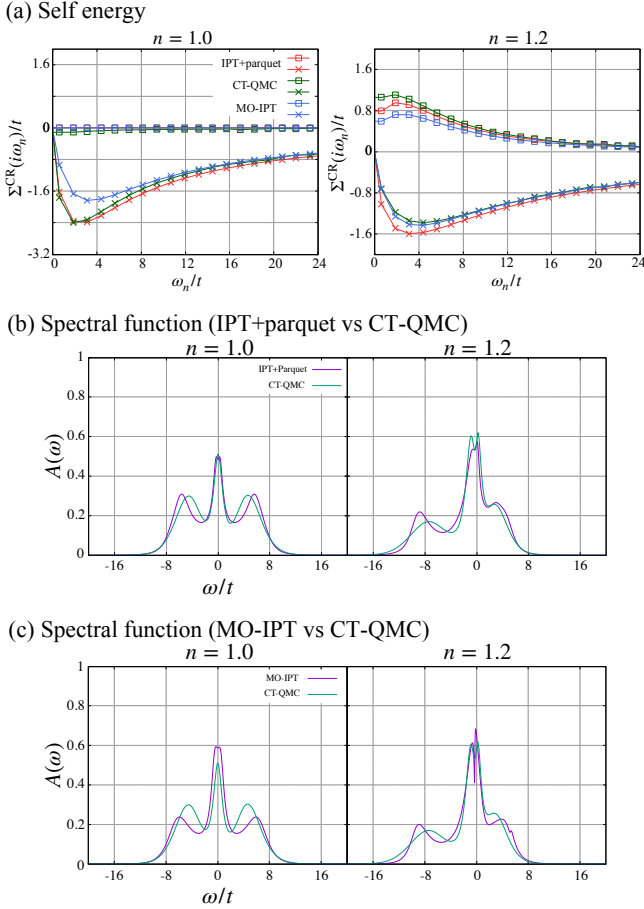


FIG. 16. (a) The correlation part of the self energy $\Sigma^{\text{CR}}(\omega)$ of the bilayer model. Square and cross symbols indicate the real and imaginary parts, respectively. Red, green, and blue lines indicate $\Sigma^{\text{CR}}(i\omega_n)$ obtained by IPT+parquet, CT-QMC and MO-IPT, respectively. (b)(c) Spectral function $A(\omega)$ of the bilayer model for several fillings. Purple lines indicate $A(\omega)$ obtained by (b)IPT+parquet and (c)MO-IPT. Green lines indicate $A(\omega)$ obtained by CT-QMC. Interaction strength is $U/t = 8$, the temperature $T/t = 0.2$, and the ratio of hoppings $t_{\perp}/t = 1.0$.

MO-IPT benchmark [22].

First, we discuss the orbital degenerate systems with the interaction having only the intra-orbital elements. The covalent insulator model in Sec. 3.3 in Ref. [22] and the bilayer model in Sec. V C in this study correspond to these systems. In these systems, both MO-IPT and IPT+parquet show good agreements with the numerically exact CT-QMC. As shown in Sec. V C, IPT+parquet (MO-IPT) is better near (away from) half-filling.

Next, we discuss the orbital degenerate systems with both intra- and inter-orbital interactions. The two-orbital Bethe lattice model in Sec. 3.4.1 and 3.4.2 of Ref. [22] and the two-orbital square lattice model in Sec. V B 2 of our study correspond to these systems. As shown in Ref. [22] and also in Sec. V B 2 of our study, the MO-IPT results significantly deviate from that of the CT-QMC results at or near half filling. This may be due to the drawback of the approximation in the modified parameter B_{α} in Eq. (31). The calculation results

lose electron-hole symmetry even in situations where the symmetry should be present since $B = 0$, which is the condition required in electron-hole symmetric systems [see Appendix B for details], is not satisfied. Another version of MO-IPT [21], which was developed by Laad *et al.* and has been applied to realistic systems [50–55], does not have this drawback. Hence, systematic benchmarks of this version of MO-IPT for simple models, which have not been performed to our knowledge, are desired. If this version of MO-IPT turns out to also give results that deviate from CT-QMC at or near half-filling, it may imply the limitations of the correction to modified parameters A, B by the static many-particle correlation functions. On the other hand, the IPT+parquet, in which the many-particle correlation effects are considered as dynamical functions obtained by the parquet equations, agrees well with CT-QMC at or near half-filling, as shown for the orbital- degenerate cases of the two-orbital square lattice and two-orbital Bethe lattice models in Sec. V B 2 and Sec. V B 1, respectively.

Finally, we discuss the orbital non-degenerate systems which correspond to the two-orbital square lattice model in Sec. V B 2 [56]. As mentioned in Sec. V B 2, a remarkable feature in this situation is that the deviations of MO-IPT from CT-QMC are largely different between the two orbitals. Namely, MO-IPT fails to appropriately describe the correlation effects near half-filling that can depend on the orbitals when the orbitals are non-equivalent. This can be understood from the viewpoint of the frequency dependence of the full vertex introduced in this study. As explained in Sec. IV B 2, $n_{0\alpha} = n_{\alpha}$ needs to be satisfied to estimate the correlation effects appropriately in each orbital. However, in MO-IPT, $n_{0\alpha}$ and n_{α} do not satisfy this condition. We overcome this difficulty by adding a degree of freedom to the pseudo chemical potential μ_0 in IPT+parquet. As a result, the IPT+parquet agrees well with CT-QMC also in non-degenerate systems.

VI. RESULTS OF IPT+PARQUET+EDF

Here, we show the results of the IPT+parquet+EDF, in which the impurity problem is solved by IPT+parquet and the non-local correlation is taken into account by EDF. We perform two types of calculation: the one-shot and self-consistent calculations. In one-shot calculation, we perform only one EDF calculation after the convergence of local IPT+parquet calculation. In the self-consistent calculation, IPT+parquet and EDF calculations are repeated alternately until convergence. Then we use the following update formula for the hybridization function $\Delta(i\omega_n)$.

$$\begin{aligned} \Delta^{\text{new}}(i\omega_n) = & \Delta^{\text{old}}(i\omega_n) \\ & + \xi G_{\text{imp}}^{-1}(i\omega_n) G_{\text{dual}}^{\text{loc}}(i\omega_n) [G_{\text{imp}}(i\omega_n) + G_{\text{dual}}^{\text{loc}}(i\omega_n)]^{-1} \end{aligned} \quad (106)$$

with

$$G_{\text{dual}}^{\text{loc}}(i\omega_n) = \frac{1}{N_{\mathbf{k}}} \sum_{\mathbf{k}} G_{\text{dual}}(k), \quad (107)$$

where ξ is the mixing rate. Through this formula, the condition

$$\sum_{\mathbf{k}} G_{\text{dual}}(\mathbf{k}) = 0 \quad (108)$$

is satisfied [35, 36]. We use the quantity α_s , which denotes the largest eigen value of $-\gamma_s \tilde{\chi}_0^C$, as a probe of the non-local correlation. The spin susceptibility χ_s diverges when α_s reaches 1.

A. Single-degree-of-freedom model

We study the single-orbital square lattice model. Here, we take 32×32 k -meshes and 4096 Matsubara frequencies.

First, we study an electron-hole symmetric case, namely, we fix the band filling at $n = 0.5$ (half filling) and consider only the nearest neighbor hopping. Figure 17 shows the temperature dependence of α_s . In the one-shot calculation, the larger the interaction U is, the larger α_s is. On the other hand, in the self-consistent calculation, the tendency is reversed at lower temperatures. For larger U , we can see the suppression of the growth of α_s associated with lowering the temperature. Especially for $U/t = 8$, α_s decreases once and increases again with lowering the temperature. Figure 18 shows the spectral functions obtained from IPT+parquet and IPT+parquet+EDF (self-consistent calculation) for several temperatures. Similarly to previous studies [40, 57], we can see the pseudo gap structure caused by the spatial fluctuation at lower temperature in each interaction strength in IPT+parquet+EDF calculation while it is not seen in the IPT+parquet (local) calculation. For $U/t = 8$ in particular, the Kondo peak begins to develop at $T/t = 0.24$, where α_s shown in Fig. 17 takes its minimal value. This suggests that the suppression of α_s is caused by the formation of the Kondo singlet. Namely, when the temperature T is decreased, first, α_s [the spin fluctuation] increases. In the temperature range where the Kondo peak develops, however, the competition between the local Kondo resonance and the non-local magnetic fluctuation suppresses the growth of α_s . When T is further decreased and after the Kondo peak grows to some extent, α_s [the spin fluctuation] begins to grow again. In the case of smaller U , this effect is smaller than that of $U/t = 8$ since the localization of electrons is weak. Also, this effect is not seen in the previous study with CT-QMC solver [36]. A possible reason is as follows, although we can not make a simple comparison of α_s here and λ_{sp} in Ref. [36] since they are not exactly the same quantity. In general, the ladder approximation, which is also adopted in Ref. [36], tends to overestimate the spin fluctuation. Hence, it may be that the effects of Kondo resonance cannot be seen in the CT-QMC calculation due to the overestimation of the spin fluctuation development. On the other hand, we can see the effect of Kondo resonance in the IPT+parquet calculation since we ignore $\overline{\text{ph}}$ and $\overline{\text{pp}}$ channels of the local full vertex in EDF, namely, an overestimation due to the ladder approximation and an underestimation due to EDF may cancel each other.

Next, we study an electron-hole asymmetric case. We set $t'/t = -0.20$, $t''/t = 0.16$, where t', t'' are the second and third nearest neighbor hoppings, assuming the single-layer

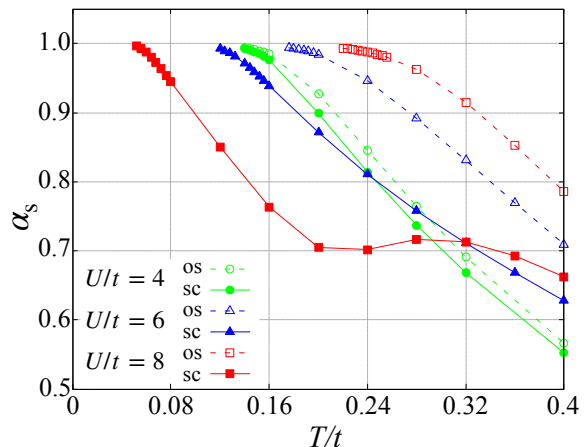


FIG. 17. The temperature dependence of α_s of the single-orbital square lattice model obtained from the IPT+parquet+EDF calculation. Green, blue, and red lines indicate the results at $U/t = 4, 6$, and 8 , respectively. Open symbols indicate the results of the one-shot (os) calculations and closed symbols the self-consistent (sc) calculations.

cuprates. The interaction strength and the temperature are fixed at $U/t = 8$ and $T/t = 0.12$, respectively. Figure 19 shows the quantity $-\text{Im}G(\mathbf{k}, i\omega_{n=0})/\pi$, which roughly corresponds to the spectral function at the Fermi level, obtained by IPT+parquet+EDF (one-shot calculation). We can see that $-\text{Im}G(\mathbf{k}, i\omega_{n=0})/\pi$ is suppressed at $(\pi, 0)$, $(0, \pi)$ in the hole-doped side ($n = 0.46$) and at $(\pi/2, \pi/2)$ in the electron-doped side ($n = 0.54$). This is consistent with the experimental results [58, 59] and the previous cluster DMFT study, in which the exact diagonalization is used as an impurity solver [60].

B. Two-orbital model

We study the two-orbital square lattice model with only the intra-orbital nearest neighbor hopping, which is the same model as in Sec. V B 2. Similarly in Sec. V B 2, we set $t_1 = t_2 = t$, where $t_\alpha = t_{i,i+1,\alpha\alpha}$ is the nearest neighbor hopping of orbital α and t is the unit of energy. The onsite energy difference is $\delta = t_{ii,11} - t_{ii,22}$, and the interactions are $U' = U - 2J$, $J = J' = U/4$. We take 32×32 k -meshes and 4096 Matsubara frequencies. Here we fix the temperature $T/t = 0.2$, the onsite energy difference $\delta/t = 1.6$, and the band filling at $n = 1.1$.

Figure 20 shows the temperature dependence of α_s of the two-orbital square lattice model for several interaction strengths. Unlike the single-degree-of-freedom case, the larger the interaction strength becomes, the larger α_s becomes in both the one-shot and self-consistent calculations. It is assumed that the Kondo resonance is weakened since the band filling is away from half filling and there exist two bands with different onsite energies. In $U/t = 6$, the difference between the results of the one-shot and self-consistent calculations is moderately large. Especially, the temperature where α_s reaches 1 in the self-consistent calculation is close to that in the case of $U/t = 4$. However, for $U/t = 8$, the difference between the results of the one-shot and self-consistent calculations is small. For this interaction strength, the band filling of the upper band is close to

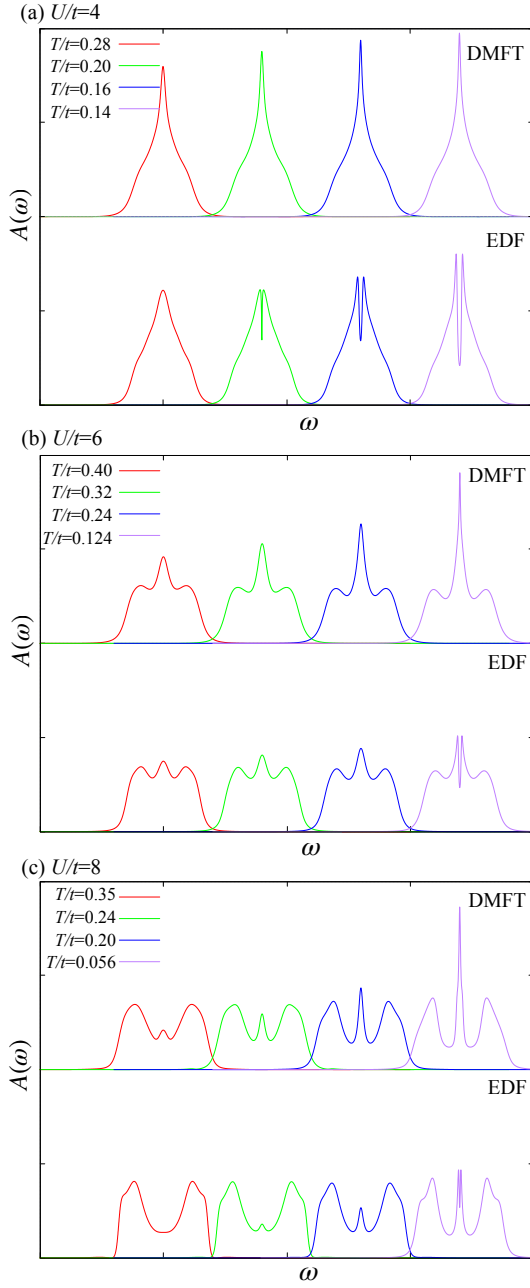


FIG. 18. The spectral function $A(\omega)$ of the single-orbital square lattice model obtained from DMFT and EDF (self-consistent). The upper panel shows the results of DMFT and the lower panel EDF. The interaction strengths are (a) $U/t = 4$, (b) $U/t = 6$, and (c) $U/t = 8$. Red, green, blue, and purple lines indicate the results at (a) $T/t = 0.28, 0.20, 0.16, 0.14$, (b) $T/t = 0.40, 0.32, 0.24, 0.124$, and (c) $T/t = 0.35, 0.24, 0.20, 0.056$, respectively.

half filling due to the Hartree shift, and hence the spin fluctuation becomes large. On the other hand, the effect of the Kondo resonance can hardly be seen in contrast to the single-orbital case.

Figure 21 shows the spectral functions obtained from IPT+parquet and IPT+parquet+EDF [self-consistent calculation] for several temperatures. For $U/t = 4, 6$, we can see the pseudo gap structure caused by the spin fluctuation at lower

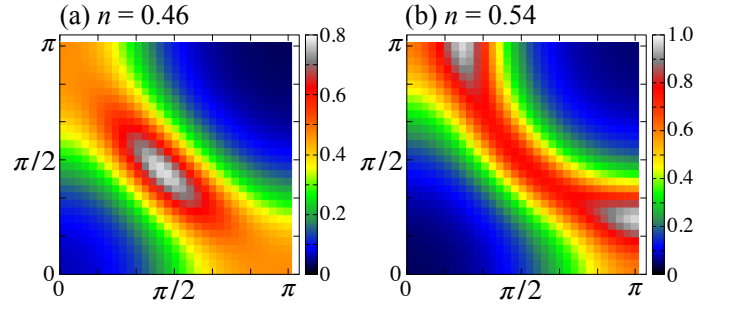


FIG. 19. The quantity $-\text{Im}G(\mathbf{k}, i\omega_{n=0})/\pi$ of the single-orbital square lattice model obtained by IPT+parquet+EDF (one-shot calculation) at the band filling (a) $n = 0.46$ and (b) $n = 0.54$. The interaction strength and the temperature are $U/t = 8$ and $T/t = 0.12$, respectively. The hoppings are $t'/t = -0.20, t''/t = 0.16$.

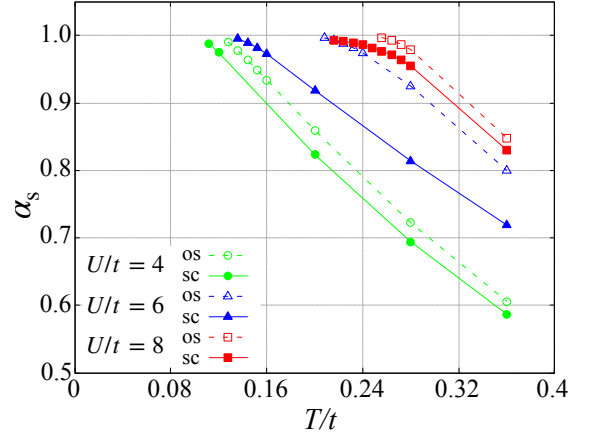


FIG. 20. The temperature dependence of α_s of the two-orbital square lattice obtained from the EDF calculation. Green, blue, and red lines indicate the results at $U/t = 4, 6$, and 8 , respectively. Open symbols indicate the results of the one-shot (os) calculations and closed symbols the self-consistent (sc) calculations.

temperatures. For $U/t = 8$, however, we can not see such a structure at any temperature. It may be because the spectrum at zero energy is indistinct even at the temperature where α_s reaches 1 for $U/t = 8$.

C. Two-site model

We study the bilayer model, which is the same model as in Sec. VC. Similarly to Sec. VC, we set the hopping ratio $t_{\perp}/t = 1.0$ and we take 32×32 k -meshes and 4096 Matsubara frequencies. Since the two sites are equivalent in this model, we show only the quantities of site 1 and omit the site index.

Figure 22 shows the temperature dependence of α_s of the bilayer model for several interaction strengths. From this figure, we can see the same tendency as in the single-degree-of-freedom case. Namely, the larger the interaction strength U is, the larger the difference between the results of the one-shot and self-consistent calculation is. However, the tendency is weaker than that of the single-degree-of-freedom case. When we compare the results of the one-shot and self-consistent

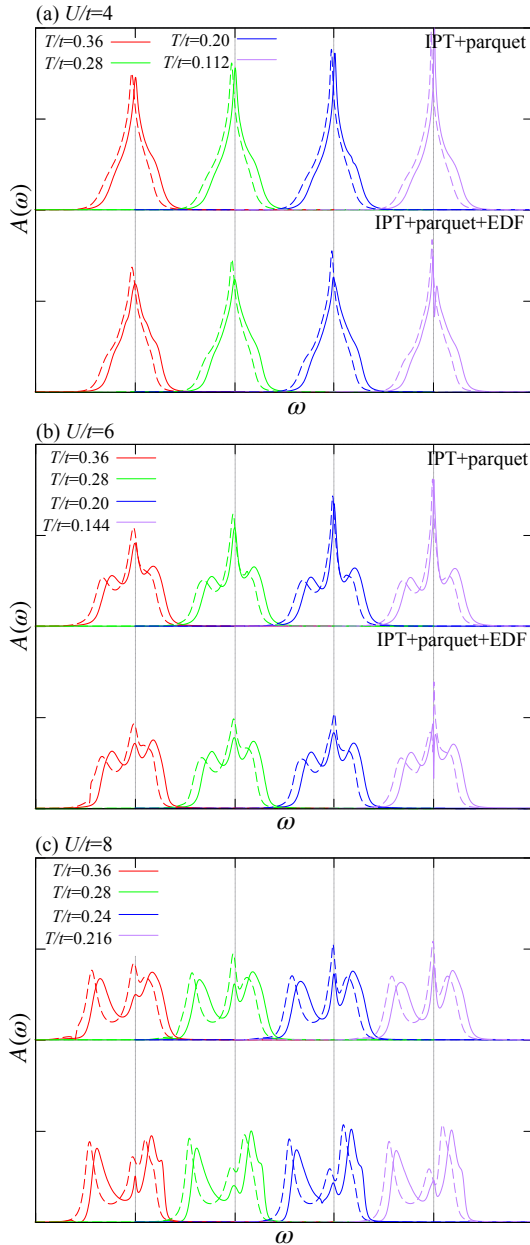


FIG. 21. The spectral function $A(\omega)$ of the two-orbital square lattice obtained from DMFT and EDF (self-consistent). The upper panel shows the results of DMFT and the lower panel EDF. The interaction strengths are (a) $U/t = 4$, (b) $U/t = 6$, and (c) $U/t = 8$. Red, green, blue, and purple lines indicate the results at (a) $T/t = 0.36, 0.28, 0.20, 0.112$, (b) $T/t = 0.36, 0.28, 0.20, 0.144$, and (c) $T/t = 0.36, 0.28, 0.24, 0.216$, respectively. Solid and dashed lines indicate the orbitals 1 and 2, respectively.

calculations, the magnitude relation of α_s 's is reversed only between $U/t = 6$ and $U/t = 8$ and α_s in $U/t = 4$ remain the smallest at any temperature. This is because the interaction strength effectively becomes smaller than that of the single-degree-of-freedom case due to the existence of the inter-layer hopping t_{\perp} .

Figure 23 shows the spectral functions obtained from IPT+parquet and IPT+parquet+EDF (self-consistent calcula-

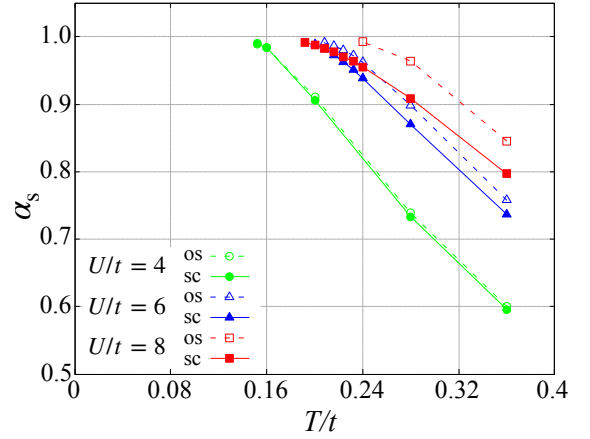


FIG. 22. The temperature dependence of α_s of the bilayer model obtained from the IPT+parquet+EDF calculation. Green, blue, and red lines indicate the results at $U/t = 4, 6$, and 8 , respectively. Open symbols indicate the results of the one-shot (os) calculations and closed symbols the self-consistent (sc) calculations.

tion) for several temperatures. We can see the pseudo gap structure at lower temperatures in all interaction strengths. In comparison with the single-degree-of-freedom case, the depth of dips between the central Kondo peak and Hubbard bands are small, so we can see that the interaction strengths are effectively small as mentioned above.

VII. RESULTS OF S2F

In this section, we show the results obtained from the calculations using the S2F method. Here, we compare three calculation procedures: IPT+parquet+EDF, IPT+parquet+S2F+EDF, and CT-QMC+S2F+EDF [we also call these three procedures by abbreviations IE, ISE, and CSE, respectively]. In IPT+parquet+S2F+EDF, we solve the impurity problem by IPT+parquet. After that, we estimate the full vertex from the self energy by S2F. Using this full vertex, we take into account the non-local correlation into DMFT solution by EDF. CT-QMC+S2F+EDF and IPT+parquet+S2F+EDF are the same except for the impurity solvers. In CT-QMC+S2F+EDF, we solve the impurity problem by CT-QMC. Results of IPT+parquet+EDF, which has already been shown in Sec. VI, are once again shown here for comparison. Also, results shown here are obtained by the one-shot calculation in terms of EDF, i.e., we perform only one EDF calculation after solving the impurity problem. Hence, no self-consistency is imposed.

Figure 24 shows the temperature dependence of α_s of three models: the single-orbital square lattice, the two-orbital square lattice, and the bilayer. First, we compare the results of IPT+parquet+EDF (IE) and IPT+parquet+S2F+EDF (ISE), which are different only in the process taking into account the spatial correlation. From Fig. 24 (a), we can see very good agreement with these two procedures in the single-orbital square lattice model. In the two-orbital square lattice model [Fig. 24 (b)], we can see the difference between the IE and the ISE at $U/t = 8$ while the difference is hardly seen at

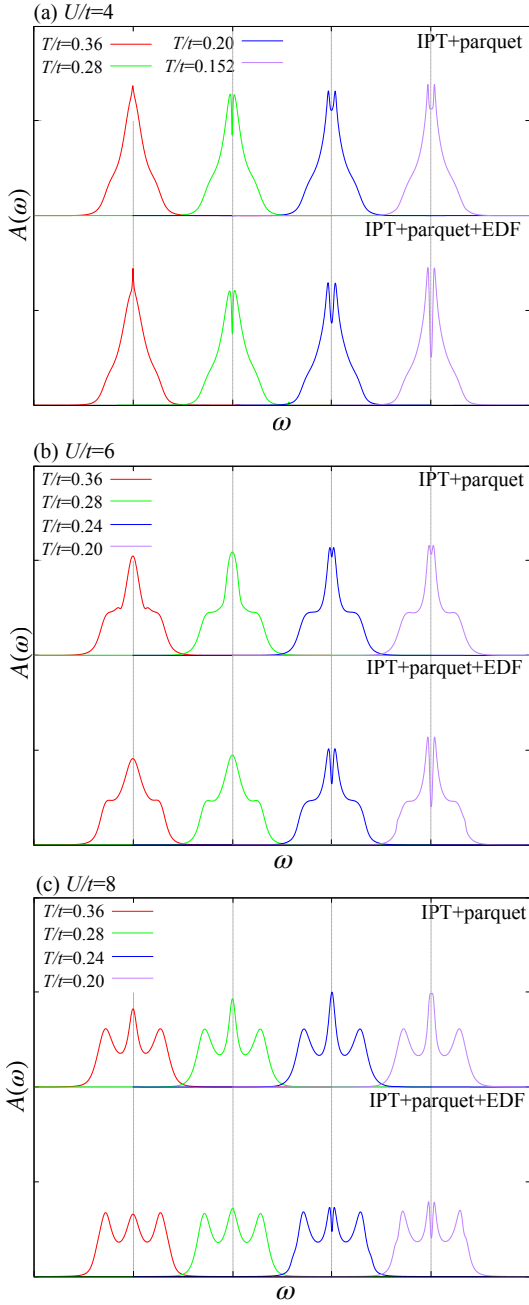


FIG. 23. The spectral function $A(\omega)$ of the bilayer model obtained from DMFT and EDF (self-consistent). The upper panel shows the results of DMFT and the lower panel EDF. The interaction strengths are (a) $U/t = 4$, (b) $U/t = 6$, and (c) $U/t = 8$. Red, green, blue, and purple lines indicate the results at (a) $T/t = 0.36, 0.28, 0.20, 0.152$, (b) $T/t = 0.36, 0.28, 0.24, 0.20$, and (c) $T/t = 0.36, 0.28, 0.24, 0.20$, respectively.

$U/t = 4$. In the bilayer model [Fig. 24 (c)], the difference between the two procedures can be seen at both interaction strengths, and especially at $U/t = 8$, ISE and IE are largely different. Note that, at present, we can not tell which of IE and ISE is better. Comparison with some numerically exact method to judge this point remain as future work. Next, we compare the results of CT-QMC+S2F+EDF (CSE) and

IPT+parquet+S2F+EDF (ISE), which are different only in the impurity solver. From Fig. 24, we can see the difference between the two procedures in all three models. α_s 's obtained from CSE are smaller than that of ISE except at $U/t = 8$ in the two-orbital square lattice model. These differences can be understood from the difference in the results of the solution of the (local) impurity problems. Except at $U/t = 8$ in the two-orbital square lattice model, the correlation effects, which can be seen in the quasi-particle weight Z for example, are smaller in CT-QMC than in IPT+parquet. Then, the full vertex which acts as the bare vertex in dual fermion system is smaller in CT-QMC than in IPT+parquet. Therefore, α_s 's in CSE are smaller than that in ISE. At $U/t = 8$ in the two-orbital square lattice model, the above relation becomes the opposite.

VIII. DISCUSSION

A. Computational efficiency

Here, we discuss the computational efficiency of the methods developed in this study. First, we compare two impurity solvers IPT+parquet and CT-QMC. We can compare the cost of IPT+parquet with that of CT-QMC since we execute calculations with both methods in this study. We employ “core hours” [61] as an indicator of numerical costs. The order of core hours of IPT+parquet is $O(1)$ and CT-QMC $O(10^2)$ in two-degree-of-freedom cases. When we consider the spatial fluctuation, the difference in the numerical costs becomes larger. Before we move on, we recall the difference between two types of extensions for spatial fluctuation, the cluster type and the diagrammatic type. In the cluster extensions, we do not have to calculate two-particle quantities, so that solving the impurity problem is not so difficult, whereas the system size is quite restricted. The cluster size is about 4 – 16 [62–64]. On the other hand, in the diagrammatic extensions, we can take large system size such as 32×32 , 64×64 , or more k -meshes [36–38], but we have to calculate the two-particle quantities. Calculating the two-particle quantities with exact impurity solvers, especially in multi-degree-of-freedom systems, is challenging. Furthermore, the reduction of the number of frequencies is indispensable to perform the calculation in a practical computational time, so that calculations at low temperatures are limited. In IPT+parquet+EDF, we can take large system sizes, easily obtain the two-particle quantities, and the reduction of the number of frequencies is not necessarily required, due to its very low numerical cost. By using S2F, in any solver, we can also overcome the difficulty in estimating the two-particle quantities.

We can roughly estimate the core hours of CT-QMC+DGA (diagrammatic type) in two-degree-of-freedom cases from the information of the previous study [65]. The core hours of CT-QMC+DGA is $O(10^4)$, while IPT+parquet+EDF $O(1)$. Furthermore, the core hour of CT-QMC+DGA increases more rapidly than that of IPT+parquet+EDF with increasing the number of Matsubara frequencies. Hence, the CT-QMC+DGA calculation is limited when the temperature is low or the degree-of-freedom of the system is large. The cost of

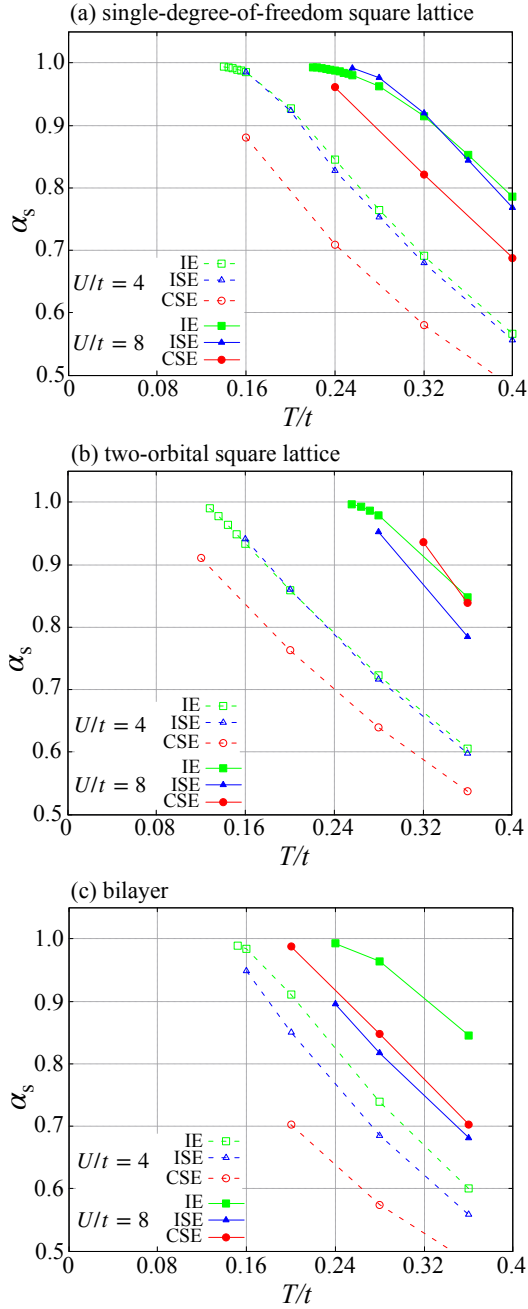


FIG. 24. The temperature dependence of α_s of (a) the single-degree-of-freedom square lattice model, (b) the two-orbital square lattice model, and (c) the bilayer model. Green, blue, and red lines indicate the results obtained by IPT+parquet+EDF (IE), IPT+parquet+S2F+EDF (ISE), and CT-QMC+S2F+EDF (CSE), respectively. Open symbols indicate the results at $U/t = 4$ and closed symbols at $U/t = 8$.

the standard dual fermion (not EDF) is assumed to be the same as DfA since the procedures of these methods are similar. The comparison of the computational efficiency between the previous methods and the newly developed methods is given in Table I. Finally, we show the computational scales of our methods. The most expensive part of IPT+parquet and S2F scales as $(N_\omega \log N_\omega)N_d^4$ and EDF as $(N_\omega \log N_\omega)(N_k \log N_k)N_d^4$, where

N_ω , N_k , and N_d are the numbers of Matsubara frequencies, k -meshes, and degrees of freedom, respectively. These estimations assume the conditions adopted in this study, in which the process of the Fourier transformation is most expensive. If N_d increases and the multiplication of two-particle quantities becomes the most expensive part, the scales of IPT+parquet and S2F become $N_\omega N_d^6$ and EDF $N_\omega N_k N_d^6$.

B. Connection to experiments

In IPT+parquet+EDF, we can obtain the two-particle quantities such as the spin susceptibility $\chi_s(\mathbf{q}, \nu)$ as well as the one-particle quantities such as the spectral function $A(\mathbf{k}, \omega)$ with high spatial resolution. The spectral function $A(\mathbf{k}, \omega)$ corresponds to the data obtained in angle-resolved photoemission spectroscopy (ARPES) and the susceptibilities $\chi_{c,s}(\mathbf{q}, \nu)$ corresponds to the data obtained in inelastic neutron scattering or the nuclear magnetic resonance (NMR). Combining the present methods with ab-initio methods, which is a future work, enables us to compare theoretical results and experimental results or to explain experimental results, even in the multi-degree-of-freedom and strongly correlated systems in which we cannot carry out calculations by conventional methods. In addition, our methods enable us to search for good conditions of physical properties such as high-temperature superconductivity in multi-degree-of-freedom and strongly correlated systems. In conventional methods, it is impossible to analyze the vast parameter (the filling, difference of energy level, correlation strength,...) space comprehensively even in systems with relatively small degrees of freedom. The methods developed in this study enables us to do this. The development of our understanding of the relation between these parameters and physical properties may lead to suggestions of novel materials.

IX. CONCLUSION

We have re-interpreted IPT from the perspective of the frequency dependence of the full vertex and extended it such that it can be applied to the multi-degree-of-freedom systems and can be combined with the extensions for the spatial fluctuations (IPT+parquet method). By using the knowledge obtained here, we have also developed two methods. One is the efficient calculation method in the dual fermion method (EDF) and the other is to estimate the two-particle full vertex from the one-particle self energy (S2F). The latter enables us to combine the extensions for the spatial fluctuation with any impurity solver. We have validated IPT+parquet by comparing it with the numerically exact CT-QMC method. As a result, we have confirmed that the results of IPT+parquet show good agreement with that of CT-QMC not only in the single-degree-of-freedom systems but also in the multi-degree-of-freedom systems. In IPT+parquet+EDF, we could have seen the pseudo gap behavior with decreasing temperature and the competition between the formation of Kondo singlet and the spatial spin fluctuation. Especially, the latter can not be seen in the one-shot calculation and so this shows the importance of the self-consistent

TABLE I. Comparison of computational efficiency.

	EIS + cluster	EIS + diagrammatic (conventional, not EDF)	IPT+Parquet + EDF	EIS + S2F + EDF
cost of impurity solver	high	high	low	high
system size	2x2 ~ 4x4	32x32, 64x64, ...	32x32, 64x64, ...	32x32, 64x64, ...
required quantity for spatial fluc.	Σ	Σ F	Σ F	Σ F

↑ difficult to calculate
↑ easy to calculate

Reduction of Matsubara frequencies N_ω is required.

↑ easy to calculate (by S2F)
 Reduction of N_ω is not necessarily required.

calculation. In the calculations with S2F procedure, we have recognized that there are differences between the results of IPT+parquet+EDF and IPT+parquet+S2F+EDF in the multi-degree-of-freedom systems. At present, we can not tell which is better. We need to compare the results with some numerically exact methods to judge this point, which is future work. Also, we have confirmed that, using the S2F procedure, we can take into account the spatial fluctuation into the CT-QMC results without directly calculating the two-particle quantities. In addition, numerical costs are largely reduced: core hours of these methods is at least 100 times smaller than that of conventional methods. We expect that our methods developed in this study can be useful for analyzing various multi-degree-of-freedom and strongly correlated systems.

ACKNOWLEDGMENTS

Part of the numerical calculations were performed using the large-scale computer systems provided by the following institutions: the supercomputer center of the Institute for Solid State Physics, the University of Tokyo, and the Information Technology Center, the University of Tokyo. This study has been supported by JSPS KAKENHI Grants No.JP18H01860.

Appendix A: Simplified parquet

In this section, we introduce the simplified parquet method in Ref. [27], in which the numerical cost is much lower than that of the non-simplified parquet method since we should practically consider just one of the three variables (k, k', q). Before we start to introduce the simplified parquet method, we define the following notation which indicates the set of the degrees of freedom, the frequencies, and wave vectors.

$$D = (\alpha, \beta, \gamma, \lambda), (k, k', q) \quad (\text{A1})$$

$$C = (\alpha, \gamma, \beta, \lambda), (k, k + q, k' - k) \quad (\text{A2})$$

$$P = (\alpha, \lambda, \gamma, \beta), (k, k', -q - k - k') \quad (\text{A3})$$

$$X = (\alpha, \gamma, \lambda, \beta), (k, -k - q, k' - k) \quad (\text{A4})$$

In the presence of SU(2) symmetry in spin space, the full vertex can be divided into four channels c(charge), s(spin),

e(even), o(odd) in terms of the parity of spin.

$$F_r(D) = \Lambda_r(D) + \Phi_{\text{ph},r}(D) + \Phi_{\text{ph},r}^-(D) + \Phi_{\text{pp},r}(D) \quad (r = c, s, e, o) \quad (\text{A5})$$

We can rewrite Eq. (A5) as follows by replacements of variables and indices.

$$F_c(D) = \Lambda_c(D) + \Phi_{\text{ph},c}(D) - \frac{1}{2}[\Phi_{\text{ph},c} + 3\Phi_{\text{ph},s}](C) + \frac{1}{2}[\Phi_{\text{pp},e} - 3\Phi_{\text{pp},o}](P) \quad (\text{A6})$$

$$F_s(D) = \Lambda_s(D) + \Phi_{\text{ph},s}(D) - \frac{1}{2}[\Phi_{\text{ph},c} - \Phi_{\text{ph},s}](C) - \frac{1}{2}[\Phi_{\text{pp},e} - \Phi_{\text{pp},o}](P) \quad (\text{A7})$$

$$F_e(D) = \Lambda_e(D) + \Phi_{\text{pp},e}(D) + \frac{1}{2}[\Phi_{\text{ph},c} - 3\Phi_{\text{ph},s}](X) + \frac{1}{2}[\Phi_{\text{ph},c} - 3\Phi_{\text{ph},s}](P) \quad (\text{A8})$$

$$F_o(D) = \Lambda_o(D) + \Phi_{\text{pp},o}(D) + \frac{1}{2}[\Phi_{\text{ph},c} + \Phi_{\text{ph},s}](X) - \frac{1}{2}[\Phi_{\text{ph},c} + \Phi_{\text{ph},s}](P) \quad (\text{A9})$$

As we can see from Eqs. (A6)–(A9), since c,s is always together with ph, e,o with pp, we omit the subscripts ph or pp hereafter. And we write the third and fourth term as $\gamma_r^{(1)}$ and $\gamma_r^{(2)}$, respectively.

We can also write the Bethe-Salpeter equation by using the four channels :

$$F_r = \Gamma_r + \Phi_r \quad (r = c, s, e, o) \quad (\text{A10})$$

$$\Phi_r = -\Gamma_r \chi_0 F_r = -\Gamma_r \chi_r \Gamma_r, \quad (\text{A11})$$

and the susceptibilities :

$$\chi_r = \chi_0 - \chi_0 \Gamma_r \chi_r = \chi_0 - \chi_0 F_r \chi_0. \quad (\text{A12})$$

With this preliminary, we will explain the details of the approximation in the simplified parquet method. First, we use the bare vertices U_r as the fully irreducible vertices Λ_r :

$$\Lambda_c(D) = (U_{\sigma\sigma\sigma\sigma} + U_{\sigma\sigma\bar{\sigma}\bar{\sigma}})(D) = U_c(D) \quad (\text{A13})$$

$$\Lambda_s(D) = (U_{\sigma\sigma\sigma\sigma} - U_{\sigma\sigma\bar{\sigma}\bar{\sigma}})(D) = -U_s(D) \quad (\text{A14})$$

$$\Lambda_e(D) = (U_{\sigma\bar{\sigma}\sigma\bar{\sigma}}^{\text{pp}} - U_{\sigma\bar{\sigma}\bar{\sigma}\sigma}^{\text{pp}})(D) = \frac{1}{2}(U_c + 3U_s)(P) \quad (\text{A15})$$

$$\Lambda_o(D) = (U_{\sigma\bar{\sigma}\sigma\bar{\sigma}}^{\text{pp}} + U_{\sigma\bar{\sigma}\bar{\sigma}\sigma}^{\text{pp}})(D) = -\frac{1}{2}(U_c - U_s)(P) \quad (\text{A16})$$

We calculate susceptibilities by using the random phase approximation (RPA) type formula :

$$\chi_r(q) = \chi_0(q)(I + \tilde{\Lambda}_r \chi_0(q))^{-1}. \quad (\text{A17})$$

where

$$\tilde{\Lambda}_r = z_r \Lambda_r \quad (\text{A18})$$

and z_r is the constant renormalization factor. With these, the irreducible vertices can be calculated as

$$\Phi_r = -\tilde{\Lambda}_r \chi_r \tilde{\Lambda}_r. \quad (\text{A19})$$

From the comparison between susceptibilities from the RPA type Eq. (A17) and the parquet type Eq. (A12), we can obtain the renormalization factor z_r as

$$z_r = 1 + \frac{\sum_{k,k',q} \chi_0(k,q)(\gamma_r^{(1)}(k-k') + \gamma_r^{(2)}(k+k'+q))\chi_0(k',q)}{\sum_q \chi_0(q)\Lambda_r \chi_0(q)}. \quad (\text{A20})$$

Although the numerator of Eq. (A20) is the sum of k, k', q , we can rewrite it the sum of q by a variable conversion. Hence, we treat only q practically. Repeating these procedure, we determine z_r self-consistently.

If we obtain the full vertex by the above procedure, we can obtain the self energy as follows.

$$\Sigma(k) = \frac{1}{4} \sum_{k'q} [F_c(D)\chi_0(k',q)U_c + 3F_s(D)\chi_0(k',q)U_s]G(k+q) \quad (\text{A21})$$

In practical calculation, however, we omit the contribution from pp channel in self energy since it tends to be overestimated and provides an unphysical result.

Appendix B: The conditions of the modified parameters in the electron-hole symmetric case

Here, we show the conditions which the modified parameters A, B need to satisfy in the electron-hole symmetric case. For simplicity, we consider the single-orbital case.

The spectral representation of the Matsubara self energy is expressed as

$$\Sigma(\omega_n) = \int_{-\infty}^{\infty} d\omega \frac{(-\text{Im}\Sigma(\omega))}{i\omega_n - \omega}. \quad (\text{B1})$$

Hence, the real part of the Matsubara self energy is

$$\text{Re}\Sigma(i\omega_n) = \int_{-\infty}^{\infty} d\omega \frac{\omega}{\omega_n^2 + \omega^2} \text{Im}\Sigma(\omega). \quad (\text{B2})$$

In the presence of the electron-hole symmetry, $\text{Im}\Sigma(\omega)$ is an even function, so $\text{Re}\Sigma(i\omega_n) = 0$.

On the other hand, the ansatz of the modified-IPT self energy is

$$\frac{A\Sigma^{2\text{nd}}(i\omega_n)}{1 - B\Sigma^{2\text{nd}}(i\omega_n)}, \quad (\text{B3})$$

where $\Sigma^{2\text{nd}}(i\omega_n)$ is the second-order self energy. In the presence of the electron-hole symmetry, the condition which A and B need to satisfy is

$$A, iB \in \mathbb{R} \quad (\text{B4})$$

since $\Sigma^{2\text{nd}}(i\omega_n)$ is a pure imaginary function. When B is real a number, B needs to be zero.

-
- [1] A. Georges, G. Kotliar, W. Krauth, and M. J. Rozenberg, *Rev. Mod. Phys.*, **68**, 13 (1996).
- [2] T. Maier, M. Jarrell, T. Pruschke, and M. H. Hettler, *Rev. Mod. Phys.*, **77**, 1027 (2005).
- [3] G. Rohringer, H. Hafermann, A. Toschi, A. A. Katanin, A. E. Antipov, M. I. Katsnelson, A. I. Lichtenstein, A. N. Rubtsov, and K. Held, *Rev. Mod. Phys.*, **90**, 025003 (2018).
- [4] A. N. Rubtsov, V. V. Savkin, and A. I. Lichtenstein, *Phys. Rev. B*, **72**, 035122 (2005).
- [5] P. Werner, A. Comanac, L. de' Medici, M. Troyer, and A. J. Millis, *Phys. Rev. Lett.*, **97**, 076405 (2006).
- [6] E. Gull, P. Werner, A. Millis, and M. Troyer, *Phys. Rev. B*, **76**, 235123 (2007).
- [7] P. Werner and A. J. Millis, *Phys. Rev. B*, **74**, 155107 (2006).
- [8] J. Otsuki, H. Kusunose, P. Werner, and Y. Kuramoto, *Journal of the Physical Society of Japan*, **76**, 114707 (2007), <https://doi.org/10.1143/JPSJ.76.114707>.
- [9] M. Caffarel and W. Krauth, *Phys. Rev. Lett.*, **72**, 1545 (1994).
- [10] D. Zgid, E. Gull, and G. K.-L. Chan, *Phys. Rev. B*, **86**, 165128 (2012).
- [11] K. Yosida and K. Yamada, *Progress of Theoretical Physics Supplement*, **46**, 244 (1970).
- [12] K. Yamada, *Progress of Theoretical Physics*, **53**, 970 (1975).
- [13] K. Yosida and K. Yamada, *Progress of Theoretical Physics*, **53**, 1286 (1975).
- [14] K. Yamada, *Progress of Theoretical Physics*, **54**, 316 (1975).
- [15] A. Georges and G. Kotliar, *Phys. Rev. B*, **45**, 6479 (1992).
- [16] H. Kajueter and G. Kotliar, *Phys. Rev. Lett.*, **77**, 131 (1996).
- [17] M. Potthoff, T. Wegner, and W. Nolting, *Phys. Rev. B*, **55**, 16132 (1997).
- [18] L.-F. m. c. Arsenault, P. Sémon, and A.-M. S. Tremblay, *Phys. Rev. B*, **86**, 085133 (2012).
- [19] T. Saso, *Journal of Physics: Condensed Matter*, **13**, L141 (2001).
- [20] T. Fujiwara, S. Yamamoto, and Y. Ishii, *Journal of the Physical Society of Japan*, **72**, 777 (2003), <https://doi.org/10.1143/JPSJ.72.777>.

- [21] M. S. Laad, L. Craco, and E. Müller-Hartmann, *Phys. Rev. Lett.*, **91**, 156402 (2003).
- [22] N. Dasari, W. R. Mondal, P. Zhang, J. Moreno, M. Jarrell, and N. S. Vidhyadhiraja, *The European Physical Journal B*, **89**, 202 (2016), ISSN 1434-6036.
- [23] Y. A. Bychkov, L. P. Gor'kov, and I. E. Dzyaloshinski, *Journal of Experimental and Theoretical Physics*, **50**, 738 (1996).
- [24] G. Rohringer, A. Valli, and A. Toschi, *Phys. Rev. B*, **86**, 125114 (2012).
- [25] V. Janiš, *Journal of Physics: Condensed Matter*, **10**, 2915 (1998).
- [26] V. Janiš, *Phys. Rev. B*, **60**, 11345 (1999).
- [27] H. Kusunose, *Journal of the Physical Society of Japan*, **79**, 094707 (2010), <https://doi.org/10.1143/JPSJ.79.094707>.
- [28] V. Janiš and P. Augustinský, *Phys. Rev. B*, **75**, 165108 (2007).
- [29] P. Augustinský and V. Janiš, *Phys. Rev. B*, **83**, 035114 (2011).
- [30] M. Potthoff, T. Wegner, and W. Nolting, *Phys. Rev. B*, **55**, 16132 (1997).
- [31] A. N. Rubtsov and A. I. Lichtenstein, *Journal of Experimental and Theoretical Physics Letters*, **80**, 61 (2004), ISSN 1090-6487.
- [32] Y. Kuramoto, *Zeitschrift für Physik B Condensed Matter*, **53**, 37 (1983), ISSN 1431-584X.
- [33] R. Bulla, T. A. Costi, and T. Pruschke, *Rev. Mod. Phys.*, **80**, 395 (2008).
- [34] A. N. Rubtsov, M. I. Katsnelson, and A. I. Lichtenstein, *Phys. Rev. B*, **77**, 033101 (2008).
- [35] A. N. Rubtsov, M. I. Katsnelson, A. I. Lichtenstein, and A. Georges, *Phys. Rev. B*, **79**, 045133 (2009).
- [36] J. Otsuki, H. Hafermann, and A. I. Lichtenstein, *Phys. Rev. B*, **90**, 235132 (2014).
- [37] D. Hirschmeier, H. Hafermann, and A. I. Lichtenstein, *Phys. Rev. B*, **97**, 115150 (2018).
- [38] E. G. C. P. van Loon, M. I. Katsnelson, and H. Hafermann, *Phys. Rev. B*, **98**, 155117 (2018).
- [39] T. Schäfer, S. Ciuchi, M. Wallerberger, P. Thunström, O. Gunnarsson, G. Sangiovanni, G. Rohringer, and A. Toschi, *Phys. Rev. B*, **94**, 235108 (2016).
- [40] H. Kusunose, *Journal of the Physical Society of Japan*, **75**, 054713 (2006), <http://dx.doi.org/10.1143/JPSJ.75.054713>.
- [41] P. Seth, I. Krivenko, M. Ferrero, and O. Parcollet, *Computer Physics Communications*, **200**, 274 (2016), ISSN 0010-4655.
- [42] P. Werner, A. Comanac, L. de' Medici, M. Troyer, and A. J. Millis, *Phys. Rev. Lett.*, **97**, 076405 (2006).
- [43] E. Gull, Ph.D. thesis, ETH Zürich (2008).
- [44] L. V. Boehnke, *Susceptibilities in materials with multiple strongly correlated orbitals*, Ph.D. thesis, Universität Hamburg (2015).
- [45] L. Boehnke, H. Hafermann, M. Ferrero, F. Lechermann, and O. Parcollet, *Phys. Rev. B*, **84**, 075145 (2011).
- [46] O. Parcollet, M. Ferrero, T. Ayrat, H. Hafermann, I. Krivenko, L. Messio, and P. Seth, *Computer Physics Communications*, **196**, 398 (2015), ISSN 0010-4655.
- [47] R. Arita and K. Held, *Phys. Rev. B*, **72**, 201102 (2005).
- [48] This is qualitatively consistent with the results of the two-orbital Bethe lattice with crystal field splitting shown in Sec. 3.5 in Ref. [22]. The situation studied in Sec. 3.5 in Ref. [22] is even further away from half-filling than $n = 1.3$ studied here. [$n_{\text{tot}} = 1.1$ in Ref. [22] corresponds to $n = 0.55$ in our study, and by electron-hole transformation, this corresponds to $n = 1.45$ in our case. The deviations of the MO-IPT results from that of CT-QMC are larger than that in Ref. [22] since the DOS of the two dimensional square lattice exhibits a van Hove singularity (in contrast to the Bethe lattice adopted in Ref. [22]), so that the quasi-particle weight is sensitive to the on-site energy difference. These results suggest that caution has to be taken when we apply the MO-IPT to systems with on-site energy difference.
- [49] D. Bergeron and A.-M. S. Tremblay, *Phys. Rev. E*, **94**, 023303 (2016).
- [50] S. Koley, M. S. Laad, N. S. Vidhyadhiraja, and A. Taraphder, *Phys. Rev. B*, **90**, 115146 (2014).
- [51] S. Koley, M. S. Laad, and A. Taraphder, *Scientific Reports*, **7**, 10993 (2017), ISSN 2045-2322.
- [52] L. Craco and S. Leoni, *Phys. Rev. B*, **100**, 121101 (2019).
- [53] M. S. Laad, L. Craco, and E. Müller-Hartmann, *Phys. Rev. B*, **73**, 045109 (2006).
- [54] L. Craco, *Phys. Rev. B*, **96**, 165412 (2017).
- [55] L. Craco and S. Leoni, *Phys. Rev. B*, **100**, 115156 (2019).
- [56] Dasari *et al.* also studied an orbital non-degenerate system in Ref. [22], where MO-IPT shows good agreement with CT-QMC for cases away from half-filling.
- [57] H. Hafermann, G. Li, A. N. Rubtsov, M. I. Katsnelson, A. I. Lichtenstein, and H. Monien, *Phys. Rev. Lett.*, **102**, 206401 (2009).
- [58] M. Horio, T. Adachi, Y. Mori, A. Takahashi, T. Yoshida, H. Suzuki, L. Ambolode, K. Okazaki, K. Ono, H. Kumigashira, H. Anzai, M. Arita, H. Namatame, M. Taniguchi, D. Ootsuki, K. Sawada, M. Takahashi, T. Mizokawa, Y. Koike, and A. Fujimori, *Nature Communications*, **7**, 10567 (2016), ISSN 2041-1723.
- [59] T. Yoshida, X. J. Zhou, K. Tanaka, W. L. Yang, Z. Husain, Z.-X. Shen, A. Fujimori, S. Sahrakorpi, M. Lindroos, R. S. Markiewicz, A. Bansil, S. Komiya, Y. Ando, H. Eisaki, T. Kakeshita, and S. Uchida, *Phys. Rev. B*, **74**, 224510 (2006).
- [60] B. Kyung, S. S. Kancharla, D. Sénéchal, A.-M. S. Tremblay, M. Civelli, and G. Kotliar, *Phys. Rev. B*, **73**, 165114 (2006).
- [61] (core hours) = (the number of CPU cores we use) \times (the number of hours for a calculation).
- [62] C. Huscroft, M. Jarrell, T. Maier, S. Moukouri, and A. N. Tahvildarzadeh, *Phys. Rev. Lett.*, **86**, 139 (2001).
- [63] E. Gull, O. Parcollet, P. Werner, and A. J. Millis, *Phys. Rev. B*, **80**, 245102 (2009).
- [64] E. Gull, M. Ferrero, O. Parcollet, A. Georges, and A. J. Millis, *Phys. Rev. B*, **82**, 155101 (2010).
- [65] A. Galler, J. Kaufmann, P. Gunacker, M. Pickem, P. Thunström, J. M. Tomczak, and K. Held, *Journal of the Physical Society of Japan*, **87**, 041004 (2018), <https://doi.org/10.7566/JPSJ.87.041004>.